STATUS REPORT
ON A
LOW-LEVEL ATMOSPHERIC TURBULENCE MODEL
FOR MARINE ENVIRONMENT

AERONAUTICAL RESEARCH ASSOCIATES OF PRINCETON, INC.
50 WASHINGTON ROAD, PRINCETON, NEW JERSEY 08540

SEPTEMBER 1976

FINAL REPORT FOR PERIOD 5 SEPTEMBER 1975 - 4 SEPTEMBER 1976

PREPARED FOR
NAVAL AIR SYSTEMS COMMAND
DEPARTMENT OF THE NAVY
WASHINGTON, D.C. 20361

D D C

OCT 19 1976

D

REPORT DOCUMENTATION PAGE	READ INSTRUCTIONS BEFORE COMPLETING FORM

1 REPORT NUMBER	2 GOVT ACCESSION NO.	3 RECIPIENT'S CATALOG NUMBER

4. TITLE (and Subtitle)	5. TYPE OF REPORT & PERIOD COVERED
STATUS REPORT ON A LOW-LEVEL ATMOSPHERIC TURBULENCE MODEL FOR MARINE ENVIRONMENT,	Final rept. 5 Sept 1975-4 Sept 1976
	6. PERFORMING ORG. REPORT NUMBER A.R.A.P. Report No. 289

7. AUTHOR(s)	8. CONTRACT OR GRANT NUMBER(s)
W.S. Lewellen, G.G. Williamson D.A. Oliver, M.E. Teske	N00019-76-C-0142 NEW

9. PERFORMING ORGANIZATION NAME AND ADDRESS	10. PROGRAM ELEMENT, PROJECT, TASK AREA & WORK UNIT NUMBERS
Aeronautical Research Associates of Princeton, Inc., 50 Washington Road Princeton, New Jersey 08540	

11. CONTROLLING OFFICE NAME AND ADDRESS	12. REPORT DATE
DEPARTMENT OF THE NAVY Naval Air Systems Command Washington, D. C. 20361	September 1976
	13. NUMBER OF PAGES 82

14. MONITORING AGENCY NAME & ADDRESS(if different from Controlling Office)	15. SECURITY CLASS. (of this report)
	UNCLASSIFIED
	15a. DECLASSIFICATION/DOWNGRADING SCHEDULE

16. DISTRIBUTION STATEMENT (of this Report)

APPROVED for public release; distribution unlimited

17. DISTRIBUTION STATEMENT (of the abstract entered in Block 20, if different from Report)

18. SUPPLEMENTARY NOTES

19. KEY WORDS (Continue on reverse side if necessary and identify by block number)

Planetary boundary layer
Turbulence modeling
Thermal radiation modeling
Sea-breeze circulation
Diurnal variations in atmospheric boundary layer

Low-level cloud dynamics
Marine atmospheric boundary layer

20. ABSTRACT (Continue on reverse side if necessary and identify by block number)

Two major modifications to A.R.A.P.'s program for computing the detailed low-level atmospheric distributions of velocity, temperature, moisture, refractive index, and the turbulent variances of these quantities for marine environments are described. The dimensions of the program have been extended to a two-dimensional, unsteady calculation to permit prediction of shoreline conditions developing in time. Also, a thermal

DD FORM 1 JAN 73 1473 EDITION OF 1 NOV 65 IS OBSOLETE

20. cont'd

radiation model has been incorporated into the one-dimensional
model to permit the radiative flux divergence term to be
computed in a fully coupled manner. Sample calculations have
been made both to verify that the program behaves in a reason-
ably physical manner and to exemplify some of the types of
boundary layer distributions which may be expected to occur.
The coupled thermal radiation model was used to make calcula-
tions of the typical diurnal variations in the boundary layer
over both land and water. The time variation of the boundary
layer's stability is quite different over water than it is over
land. This leads to sea-breeze circulations in the coastal
planetary boundary layer which are exemplified in calculations
using the two-dimensional, unsteady version of the model.

ACCESSION for

NTIS   White Section   ☑
DDC   Buff Section   ☐
UNANNOUNCED   ☐
JUSTIFICATION ....

....

BY . . . .
DISTRIBUTION/AVAILABILITY CODES

Dist   . . . . . of SPECIAL

OCT 19 1978

D

TABLE OF CONTENTS

I. INTRODUCTION

This report describes the progress made over the past year
toward the development of a program for computing the detailed
low-level atmospheric distributions of velocity, temperature,
moisture, refractive index, and the turbulent variances of these
quantities for marine environments. The program is designed to
provide the capability of taking the predicted output of a large-
scale meteorological forecast model, such as that developed at
Fleet Numerical Weather Central, and using this as boundary condi-
tions to make predictions of the detailed microstructure of the
planetary boundary layer at desired locations. This program
development also provides a means for checking and upgrading the
boundary layer parameterization used in the global forecast model
which should ultimately permit an improved accuracy in the large-
scale forecast.

Our approach to this program has been to use the invariant
second-order closure model of turbulence developed by Dr. Coleman
duP. Donaldson and his associates at A.R.A.P. over the past few
years. The fundamentals of this approach are given in Ref. 1. A
review of the status of this model as applied to a wide variety of
turbulent flow problems is given in Part II of Ref. 2. Particular
applications of the model as applied to atmospheric problems,
including comparisons with experimental data, are documented in
Refs. 2-6.

Reference 7 is a technical report detailing the model develop-
ment, sample calculations, and verification comparisons made under
our initial contract. It describes the addition of humidity and
the second-order turbulent correlations involving humidity as
variables to our dry atmospheric boundary layer program previously
developed for the Environmental Protection Agency. These variables
were added without the need to add any new coefficients to the
model by observing that in the limit of vanishingly small fluctua-
tions in either humidity or temperature both are transported as
passive quantities and thus should be modeled similarly. The

different influence of humidity and temperature on buoyant pro-
duction of turbulence is included explicitly in the equations
for the turbulence, with no need to model these terms. Verifi-
cation of the model predictions for humidity transport were made
by comparison with evaporation experiments in a wind tunnel
(Ref. 8).

The boundary conditions at the surface of the earth were
modified to provide for appropriate coupling to the sea state
by using Froude number scaling following Wu (Ref. 9) to provide
a relationship between the effective aerodynamic roughness of
the sea surface and the surface shear stress velocity. This
allows both the low-level wind distribution and the surface
roughness to be determined by the model.

The total water content, liquid plus gas, is transported by
the turbulence. Provision for the water content to change its
phase has been made by assuming that when both liquid and water
vapor coexist their relative proportion is determined by equili-
brium saturation conditions. The heat released in the conden-
sation process is included in both the mean average temperature
equation and in the correlation equations involving temperature
fluctuations.

Using the predicted distributions of temperature, humidity,
and pressure, a calculation of the modified refractive index, M,
has been incorporated in the program. Local minimums in the M
distribution with respect to altitude directly indicate the
presence of a radar duct. Since we are predicting the second-
order correlations between the turbulent fluctuations in tempera-
ture and humidity as well as the average scale of the turbulence,
we have available the information to also compute the structure
of the fluctuations in refractivity.

Reference 7 includes the results of several sample calcu-
lations; e.g.: (a) a sample calculation using output from FNWC
(supplied by J. Kaitala) as upper and surface boundary conditions
for our boundary layer program; (b) a comparison of predicted

temperature structure parameters with the observations of
Wyngaard, et al. (Ref. 10); (c) a calculation with boundary
conditions roughly corresponding to the conditions observed in
the Atlantic Tradewind Experiment by Augstein, Schmidt, and
Ostapoff (Ref 11); and (d) a calculation simulating shoreline
conditions for either a dry land breeze over the sea or a moist
sea breeze over dry land.

This report describes two major modifications to the model
described in Ref. 7. These are: (a) the increase in the dimensions
of the program to a two-dimensional, unsteady calculation to per-
mit the prediction of shoreline conditions developing in time, and
(b) the incorporation of the radiative flux divergence term into
the one-dimensional system of equations in a coupled manner. The
numerical developments required to extend the program to two di-
mensions are discussed in the next section.

The radiation model coupled into the one-dimensional, boundary
layer model is described in Appendix A. The incorporation of a
coupled radiation model is important under stable atmospheric con-
ditions when the comparative ratio of the divergence of radiation
heat flux to that of the turbulent heat flux may reach order one.
The primary coupling between the turbulent transport and radiation
comes through the humidity distribution. The water vapor content
has a strong influence on the long-wave radiative cooling, while
the liquid water content is the most dominating factor in the
short-wave radiative heating. Verification comparisons with
observational data are included in Appendix A.

We have also made some modifications to the condensation
algorithm to provide for a transition regime between the completely
unsaturated and completely saturated regimes. The need for and
consequences of this modification are discussed. Calculations have
been made both to verify that the modified program behaves in a
reasonable fashion and to exemplify some of the types of boundary
layer distributions which may be expected to occur.

Sample calculations of the diurnal variation in the planetary boundary layer over both land and water have been calculated with detailed thermal radiation coupling. The conditions for the calculation over land are picked to correspond to that for a typical midwestern summer day previously calculated ignoring radiation coupling and published in Refs. 2 and 4. This permits the significance of the radiation coupling for such a calculation to be directly assessed. A sample calculation over a boundary layer over water is then presented to show the interaction between radiation, cloud dynamics, and turbulence. These two sample diurnal variation calculations clearly show that the time variation of the boundary layer's stability is quite different over water than it is over land.

Finally, the two-dimensional, unsteady version of the model has been used to calculate the typical variation in the coastal planetary boundary layer. The results of this calculation have been written for presentation at the AMS Conference on Coastal Meteorology to be held at Virginia Beach, September 21-23, 1976. This paper is included as Appendix B to this report. The resulting diurnal variation in the sea breeze induced by the strong stability differences in the boundary layer response over the land and that over the water produces a strong asymmetry between the sea-breeze and the land-breeze circulation patterns. In previous sea-breeze models it was necessary to impose eddy viscosities which were a strong function of time and space to gain this asymmetry. In the present model it is achieved without the need to introduce any new empirical information.

II. MODEL EXTENSION

Two major modifications to the model have been made. The
numerics of the model have been extended to permit two-dimensional,
unsteady calculations, and a radiative flux divergence calculation
has been added to the one-dimensional system of equations to permit
a direct coupling between the distributions of temperature and
water vapor predicted by turbulent transport and the radiative
energy source.

The only other change to the model during the past year has
been a refinement in our condensation algorithm to provide for a
transition regime between the completely unsaturated and completely
saturated regimes. Sample calculations had shown that this was
desirable to simulate conditions corresponding to scattered cloud-
iness. The new algorithm permits condensation to be influenced by
the turbulent fluctuations in H and H_s as well as by their
ensemble-average value.

The development and verification of the radiation model are
given in Appendix A.

2.1 Program Extension to Two Dimensions

To include the physics generated by the true ellliptic nature
of the shoreline sea-breeze problem, we must allow additional
variation in the direction normal to the shore. The program used
to develop the solutions discussed later and in Appendix B is an
extension of a computer program developed with the support of EPA
through our continuing turbulent modeling effort. This program
initially solved for the primitive variables (W, H, θ_v, U, V) and
the turbulence in the y-z computational mesh in a time-dependent
mode. In this scheme, the vertical velocity W was obtained using
the boundary layer approximations so that it was solved by quadra-
ture from the horizontal velocity V through continuity. A review
of the solution process may be found in Ref. 2.

To complete the sea-breeze circulation, it is necessary to
provide a consistent W boundary condition at the top of the

simulation domain. The use of the continuity equation to determine W allows the use of only one boundary condition (namely, $W = 0$ at $z = 0$) and forces W to be nonzero at the top of the computational domain. To permit the imposition of $W = 0$ at the top (and thereby closing the domain), we developed a hybrid solution scheme involving the streamfunction ψ. The horizontal velocity V is solved at each time step by the horizontal momentum equation. The vorticity is found by differentiating V in the vertical direction; the streamfunction ψ is obtained by a direct solution of Poisson's equation using the solver developed by Swarztrauber and Sweet (Ref. 12). The top boundary value of ψ is taken as constant, forcing W to be zero along the top boundary. The vertical momentum equation provides the equation for the hydrostatic pressure. The resulting horizontal pressure gradients are the forcing functions for the sea-breeze circulation.

The greatest difficulty in the numerics of this two-dimensional, unsteady system is associated with the internal waves in the region of the stable temperature inversion. Since these stable potential temperature gradients can become relatively strong at the top of the mixed layer, the characteristic Brunt-Väisälä period can be of the order of tens of seconds. Since the full turbulent correlation equations follow these waves, it is necessary to run with very small time increments. This makes a full day's simulation of the two-dimensional coastal boundary layer unduly lengthy. To circumvent this problem, the sample calculations shown here and in Appendix B have been run with upwind-differencing and with quasi-equilibrium turbulence. Upwind-differencing introduces some numerical damping into the calculation so that larger time steps may be taken. The quasi-equilibrium turbulence approximation is detailed in Ref. 2. The basic approximation is to drop out all time derivative and diffusion terms in the second-order correlation equations, except in the q^2 equation. This has the desirable effect of filtering out the wave dynamics from the correlation equations. The penalty for this is some loss in the faithfulness with which the equations model the turbulence.

6

We cannot give a precise bound on the errors introduced into the calculation by these approximations but believe that, at least, the qualitative behavior of the results is correct. Definitive accuracy estimates must await comparison with reliable field data.

It should perhaps be restated here that the two-dimensional program does not currently have either the coupled radiation calculation or the condensation algorithm included. These two physical phenomena are being checked out in the simpler one-dimensional program before inclusion into the two-dimensional system.

Figure 1 demonstrat. the difference between the results of a two-dimensional, elliptic calculation for the shoreline boundary layer and that of a two-dimensional, parabolic calculation in even the steady case. For this calculation, the geostrophic wind is assumed to be directed normal to the shore with the water temperature $11°C$ cooler than the land. The inflow conditions are held constant at conditions corresponding to a typical quasi-steady boundary layer over water with an inversion height of approximately 1500 m.

This problem may be solved using the one-dimensional program by assuming that the flow is parabolic and marching in the direction normal to the shoreline. The contours of constant turbulent kinetic energy obtained in this way are shown in Fig. 1-a. This calculation does not permit any influence of recirculations. Figure 1-b shows the corresponding variable as predicted by the two-dimensional elliptic calculation. This is obtained by starting the two-dimensional calculation with the conditions obtained from the parabolic calculation and then marching in time until a type of steady state is reached. Figure 1-b shows more structure than can be observed in Fig. 1-a. Figure 1-c is the qualitative field observations as obtained from multiple passes with an aircraft (Ref. 13) along the shore of Lake Michigan. The value of the geostrophic wind at the time of their flight is not specified, so it is not possible to make a quantitative comparison. The height
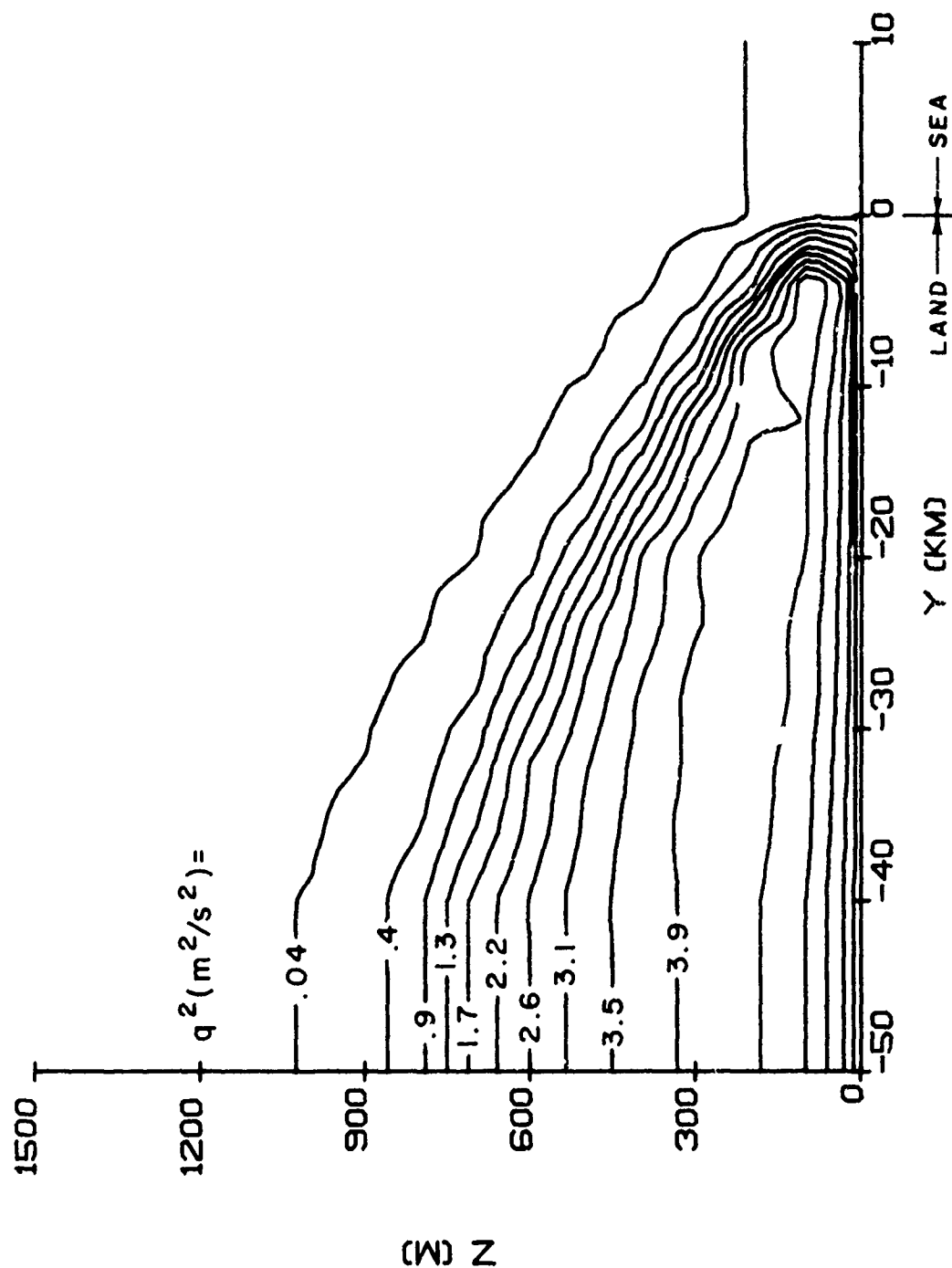
Figure 1-a. Boundary layer growth in turbulent kinetic energy along the shoreline with the geostrophic wind from the water at 10 m/sec and the land warmer than the water: parabolic calculation.
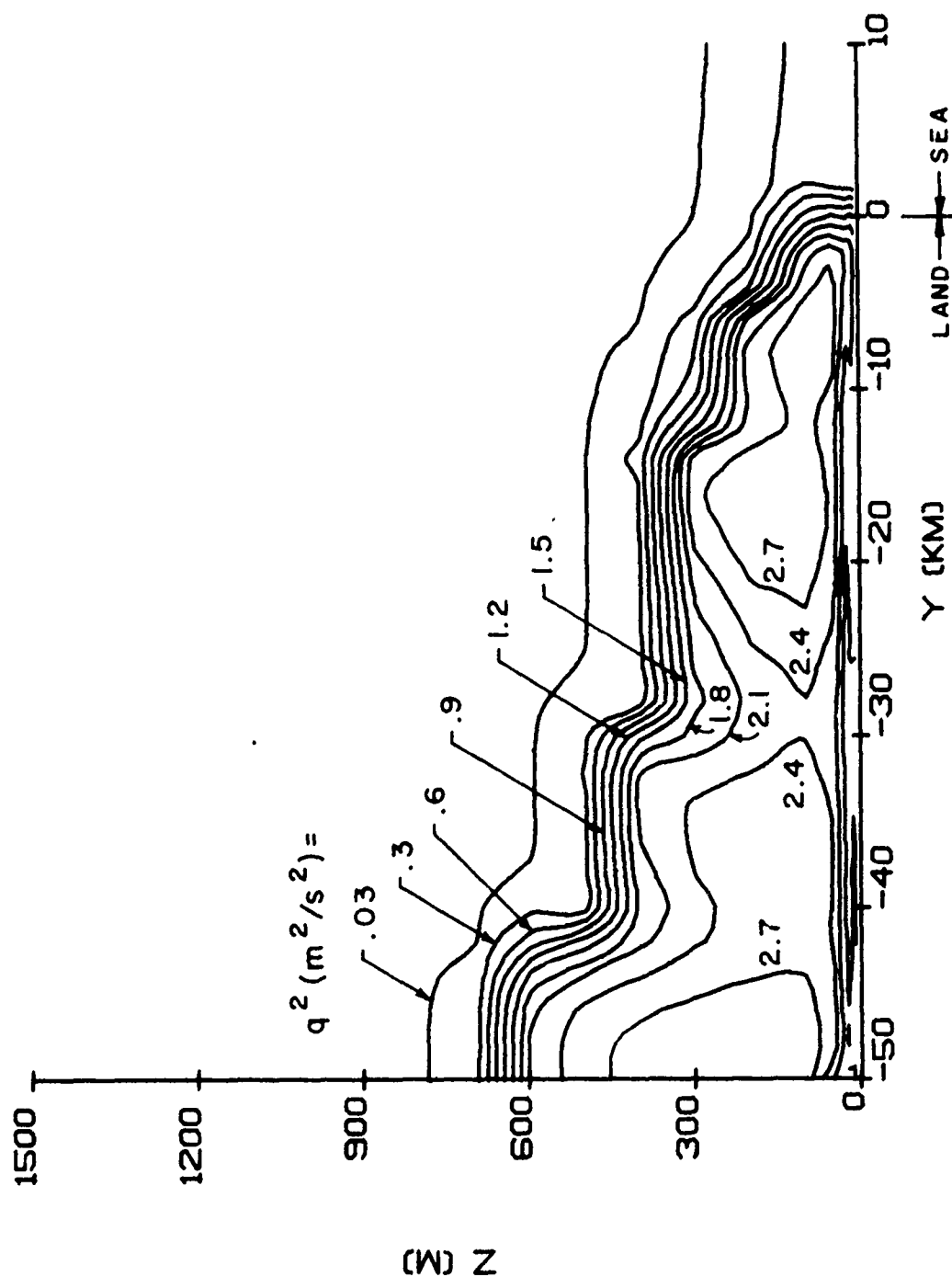
8

Figure 1-b. Boundary layer growth in turbulent kinetic energy along the shoreline with the geostrophic wind from the water at 10 m/sec and the land warmer than the water: elliptic calculation.

9

I Slight "cobblestone" motion
II Noticeable bouncing
III Typical daytime low level turbulence
IV Greater than normal/occasionally moderate

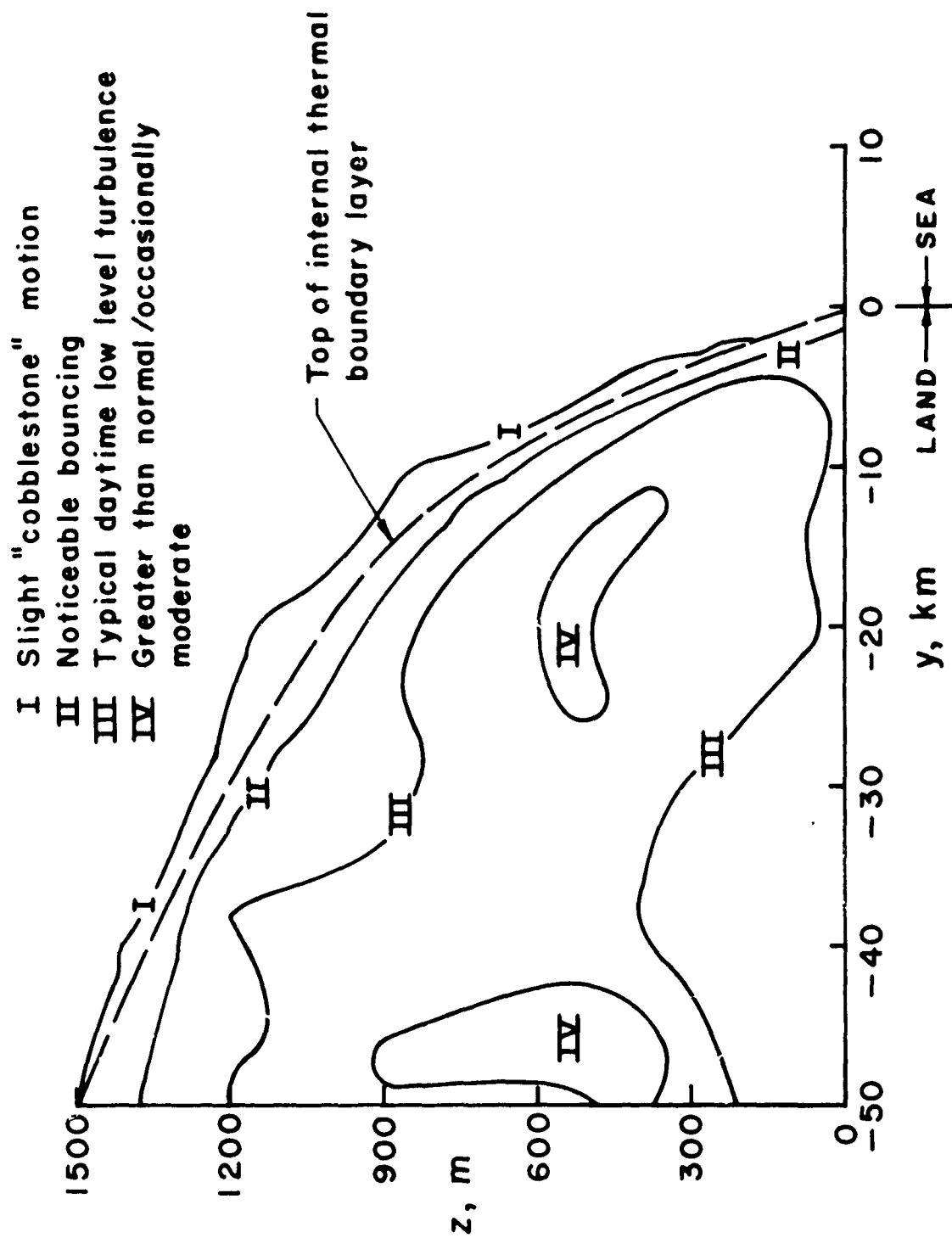Top of internal thermal boundary layer

z, m

y, km

LAND ⊣ SEA

Figure 1-c. Boundary layer growth in turbulent kinetic energy along the shoreline with the geostrophic wind from the water at 10 m/sec and the land warmer than the water: qualitative observations from Ref. 13.

of the boundary layer thickness at 50 km inland would increase
if the geostrophic wind were decreased for a specified temperature
difference between the land and the water. We did use the same
temperature difference in the calculation as was specified in the
observations.

Both the elliptic predictions and the observations show, at
least qualitatively, the same structure to the turbulent kinetic
energy field. The local maximum in q^2 nearest to the shoreline
is predicted by both the elliptic and the parabolic calculation.
This increase in turbulence is caused by the increased shear stress
and heat flux in the internal boundary layer which begins at the
shoreline. As the new boundary layer increases in thickness, the
shear decreases and, consequently, so does the turbulent kinetic
energy. The added detail of the local recirculations appears to be
necessary to predict the second local maximum in q^2. The vertical
potential temperature contours for this flow are shown in Fig. 2.
Again, the undulating character of the boundary layer growth is
clearly in evidence. As previously explained, the results of this
computation cannot be used to quantitatively verify the program,
but it does show that the results are at least qualitatively correct.

2.2 Turbulent Contribution to Condensation

As detailed in Ref. 7, the change of phase of water was
originally taken as entirely governed by the mean values of $\bar{H}$ and
$\bar{H}_s$. As explained there, we were relying on turbulent diffusion
in the equations to smooth out the transition between saturated
and unsaturated conditions. Under conditions when light, scattered
clouds might be anticipated, this appeared to cause some problems.
The program attempted to compensate for its inability to specify
spatially scattered clouds by prescribing a birth and decay of
clouds in time over a period of the order of minutes.

Under the assumption of equilibrium condensation, the change
of phase should be governed by the instantaneous values of H and
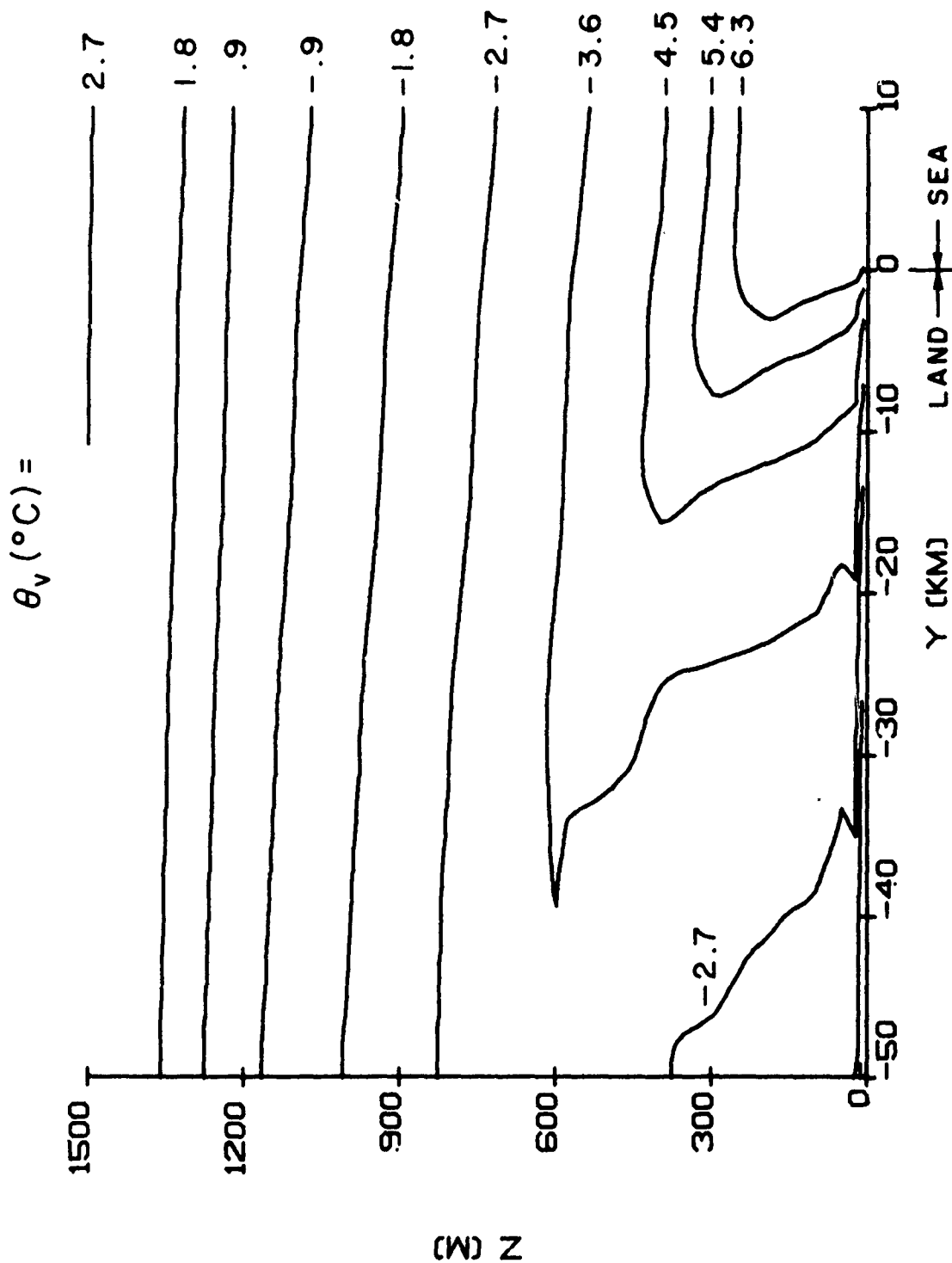H_s. Since liquid water content ξ is physically a positive

11

Figure 2. Virtual potential temperature contours for the flow of Figure 1 as predicted by the elliptic calculation.

12

definite quantity, it may be seen that the contributions made
when $\bar{H} + H' > \bar{H}_s + H'_s$ cannot be balanced by contributions from
$\bar{H} + H' < \bar{H}_s + H'_s$. Thus,

$$\bar{\xi} = \bar{H} - \bar{H}_s \tag{1}$$

only when the flow is sufficiently saturated that no local unsatu-
rated region is contained within an eddy.

To approximately account for this phenomenon, we have added a
transition regime between the completely unsaturated and completely
saturated regimes. This occurs when the fluctuations in H and
H_s may be large enough to make the sign of $H - H_s \neq$ to the sign
of $\bar{H} - \bar{H}_s$. By letting the fluctuations be characterized by their
rms values, the transition regime may be defined as occurring
whenever

$$\left(\overline{H'^2}\right)^{1/2} + \left(\overline{H'^2_s}\right)^{1/2} \geq |\bar{H} - \bar{H}_s| \tag{2}$$

To precisely specify the liquid water content in this regime, it
would be necessary to know the distribution of H' and H'_s about
$\bar{H}$ and $\bar{H}_s$. Since this is more information than is possible in
a model based on ensemble averages, we will approximate the average
liquid water content in this region as

$$\xi = \frac{1}{2}\left[\bar{H} - \bar{H}_s + \left(\overline{H'^2}\right)^{1/2} + \left(\overline{H'^2_s}\right)^{1/2} \right] \tag{3}$$

Equation (3) has the correct limits of zero and $\bar{H} - \bar{H}_s$ when the
equal sign in Eq. (2) holds. Further, when $\bar{H} = \bar{H}_s$ and H' (or
H'_s) is zero, it recognizes that only negative H'_s (or positive
H') will lead to condensation.

The coefficients K_1 , related to the effective increase in
the specific heat capacity of the mixture due to change of phase,
and K_2 , the effective change in the neutral lapse rate due to

13

change of phase, are assumed to vary linearly between their saturated and unsaturated values in direct proportion to the liquid water content. If K_{1_S} and K_{2_S} are specified as the saturated values of these coefficients, as given in Eq. (32) of Ref. 7, then in the new transiton regime

$$K_1 = 1 + \left(K_{1_S} - 1\right) \bar{\xi} \Big/ \left[\left(\overline{H'^2} \right)^{1/2} + \left(\overline{H_S'^2} \right)^{1/2} \right] \tag{4}$$

$$K_2 = K_{2_S} \bar{\xi} \Big/ \left[\left(\overline{H'^2} \right)^{1/2} + \left(\overline{H_S'^2} \right)^{1/2} \right] \tag{5}$$

Fluctuations in the saturated value of humidity are related to fluctuations in temperature through the Clasius-Clapeynon equation. For small fluctuations, this gives

$$H_S' = \frac{T'}{T} \frac{H_S L}{R_V T} \tag{6}$$

Thus, in terms of the virtual potential temperature which is used in the program

$$\left(\overline{H_S'^2} \right)^{1/2} = \frac{L H_S}{R_V T} \left[\frac{\overline{\theta_v'^2}}{T_\infty^2} - 1.22 \frac{\overline{H'\theta'}}{T_\infty} + (0.61)^2 \overline{H'^2} \right]^{1/2} \tag{7}$$

This completes the specification of the condensation model. The influence of this modification will be discussed in connection with the sample calculation of the marine atmospheric boundary layer in the next section.

III. SAMPLE CALCULATIONS

This section contains the results of sample calculations for the atmospheric boundary layer over either land or water to demonstrate the strong difference which occurs in the diurnal variations in these two types of boundary layers. The resulting differences in the boundary layer response over the land and over the water present the opportunity for a sea-breeze circulation along any coast. Appendix B presents the results of a sample calculation of this phenomenon.

3.1 Diurnal Variation Over Land with Detailed Thermal Radiation Coupling

In previous simulations (2 & 4) of the diurnal variation in the planetary boundary layer, the A.R.A.P. second-order closure turbulence model was utilized with a simple ad hoc radiation loss term representing long wavelength cooling of the boundary layer. Direct solar heating was neglected. This radiation loss term was assumed known as a function of time and space. We now present a prediction of the diurnal cycle utilizing the full second-order closure model described in Ref. 7, but with the detailed thermal radiation model described in Appendix A. We consider the diurnal variation near relatively dry land for conditions driven by the surface heat flux measured in Kansas for a three-week period in summer and summarized by Wyngaard (Ref. 14). We shall compare the present calculations utilizing the detailed radiation model with the calculation for the identical Kansas data reported in Refs. 2 and 4 utilizing an assumed radiation cooling which was uniform in time and represented by either a uniform or cosine variation over space from the surface to the top of the boundary layer. For the present calculation, the surface humidity mixing ratio is held at 0.01 unless the saturation value falls below this value, in which case it is set equal to the local saturated value. The previous runs were independent of humidity.

15

The behavior over the diurnal period is briefly as follows. Beginning at sunrise, surface heating destabilizes the lower boundary layer and turbulence production becomes intense over the daytime period. Maximum turbulent kinetic energy densities are reached at about 2 p.m. in the range of 600-1200 m (Fig. 3). Turbulence begins to subside after 3 p.m. in the afternoon and has fallen to a very low level by 9 p.m. in the evening. Because of the viscous coupling with the upper geostrophic wind, the coriolis-driven wind component normal to the geostrophic is closely coupled to geostrophic during the day (deviation approximately $6°$) and swings away from the geostrophic during the quiescent night period by about $37°$ maximum. As the surface cools at night, a low-level inversion in temperature forms above the surface. The cool surface also induces a slight nocturnal jet.

These general diurnal phenomena have been predicted both by the model with approximate radiative loss (Ref. 2) and by the present model with detailed thermal radiation. The detailed radiation model, however, introduces some quantitative modifications. The most significant change brought about by detailed inclusion of thermal radiation is in the diurnal variation in the near surface temperature (Fig. 4). With only an overall radiative loss model, the surface temperature cools to an un-realistically low level during the night, reaching a maximum of about $-3°C$ in potential temperature just before sunrise. With detailed inclusion of radiation, the surface is actually radi-atively heated during the night by the lower warm, humid air layers in the 0-200 meter altitudes. The high humidity of the summer midwestern atmosphere renders it optically quite thick to thermal radiation; hence, the lower air layers effectively blanket the surface from direct cooling to space and lead to a much more realistic minimum in surface temperature of $19°C$ just before sunrise. These results, of course, manifest the f(c ι .c during the relatively quiescent night the radiative heat , ˙: as important as the turbulent fluid heat flux.
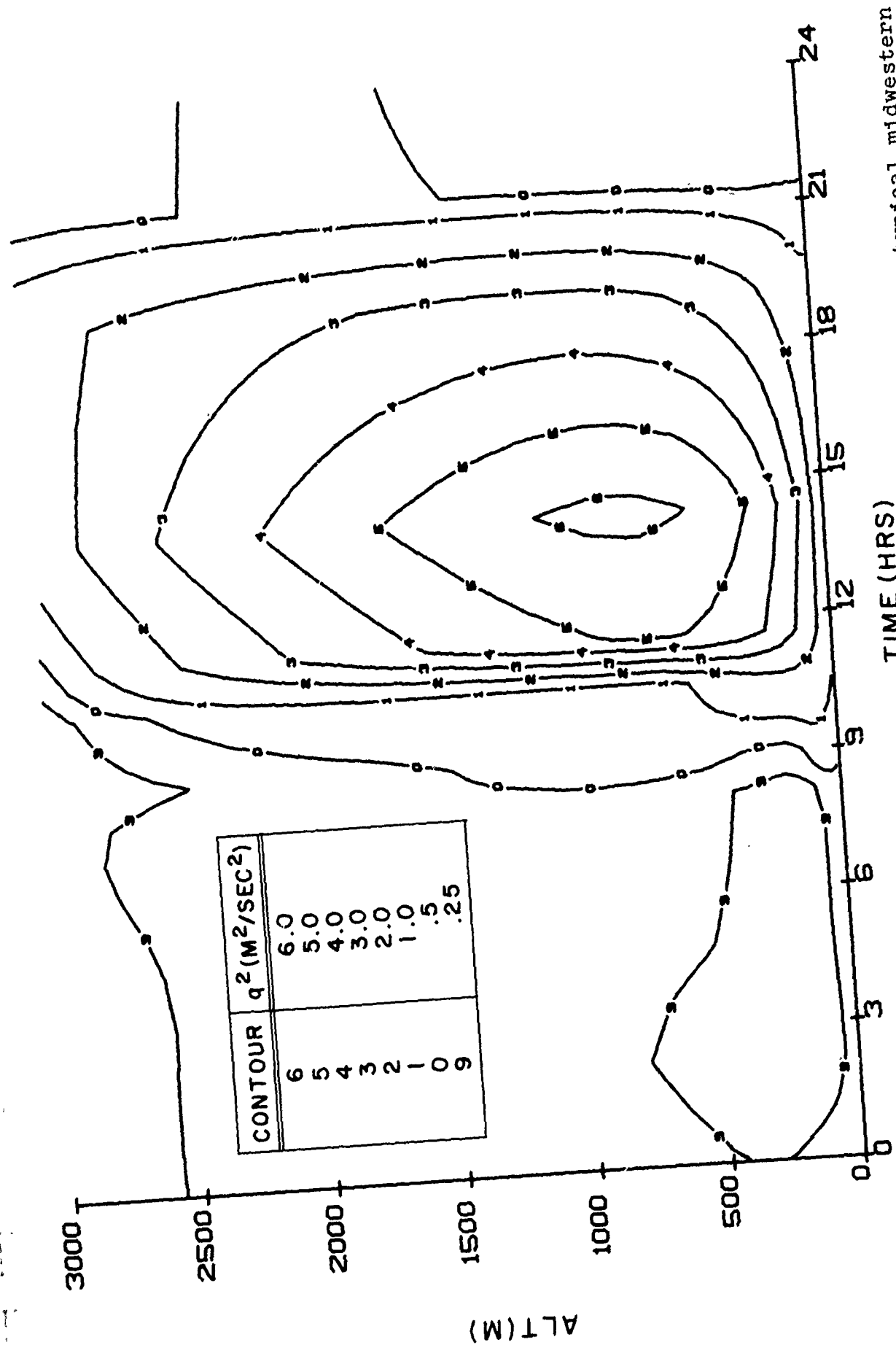
Figure 3. Turbulent kinetic energy as a function of time and altitude for a typical midwestern summer day; computed with detailed radiation coupling.
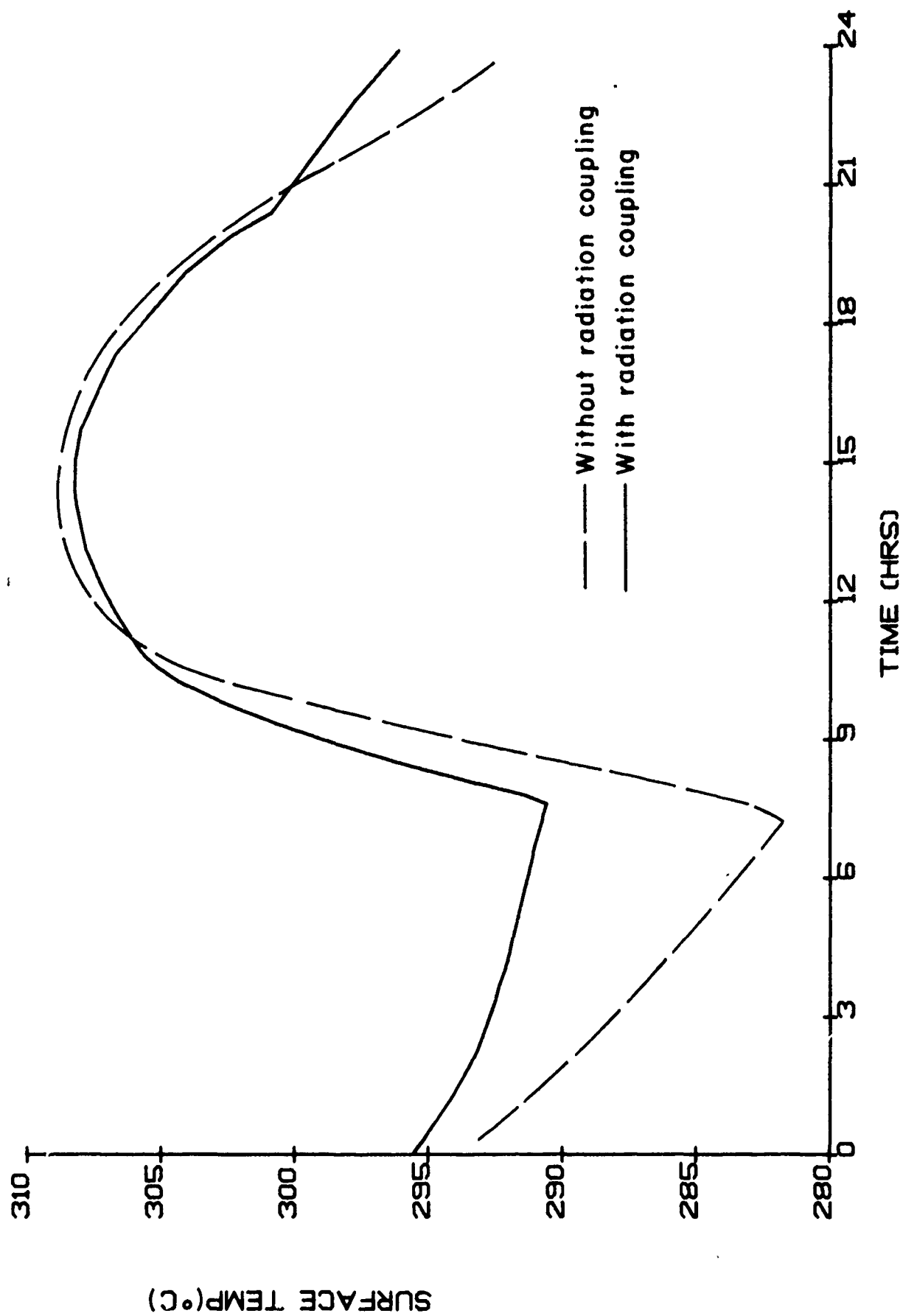
CONTOUR	$q^2(M^2/SEC^2)$
6	6.0
5	5.0
4	4.0
3	3.0
2	2.0
1	1.0
0	.5
9	.25

TIME (HRS)

ALT (M)

Figure 4. Surface temperature variation as a function of time for a typical midwestern summer day with and without radiation coupling.

- - - Without radiation coupling

——— With radiation coupling

18

The temperature profiles and radiative heating/cooling rate profiles undergo significant structural changes over the diurnal period. In Fig. 5-a, the state in early morning before sunrise is shown. The lower level temperature inversion is near its maximum at this time, and the boundary layer is actually being radiatively heated below 200 meters and radiatively cooled to space above 200 meters. In Fig. 5-b, the state after sunrise is shown. The rapid surface heating has switched the temperature profile from one of simple inversion to one of inflection. As a result, the lowest surface layers switch to radiative cooling, the mid-layers remain in heating, and the upper layers remain in cooling. By mid-morning (Fig. 5-c), the inflection is gone and the pattern for the principal part of the day has been set in which the temperature profile decreases monotonically from the surface to the top of the boundary layer, the lower boundary layer is in radiative cooling, and the upper part of the boundary layer is in weak radiative heating due to direct solar heating slightly exceeding the long wavelength cooling during the daytime. In the early afternoon with the sun past its zenith, the upper layers switch to radiative cooling, the mid-layers remain in heating, and the lower layers in cooling (Fig. 5-d).

Interestingly, the only period during the day in which the entire boundary layer is in radiative cooling is from about 4 p.m. in the afternoon to 7 p.m. in the evening. (Recall that in the simple radiation loss model of previous calculations, the entire boundary layer was assumed to be radiatively cooling at all points in space and at all times.) In the evening (Fig. 5-e), the uniform cooling is about to give way in the formation of the nocturnal surface inversion which is well-developed by midnight (Fig. 5-f) and will strengthen to its maximum by morning just before sunrise (Fig. 5-a).

Detailed predictions of the radiation field results in a weaker stable temperature profile during the night. As a result, the overall diurnal variation is somewhat more turbulent with
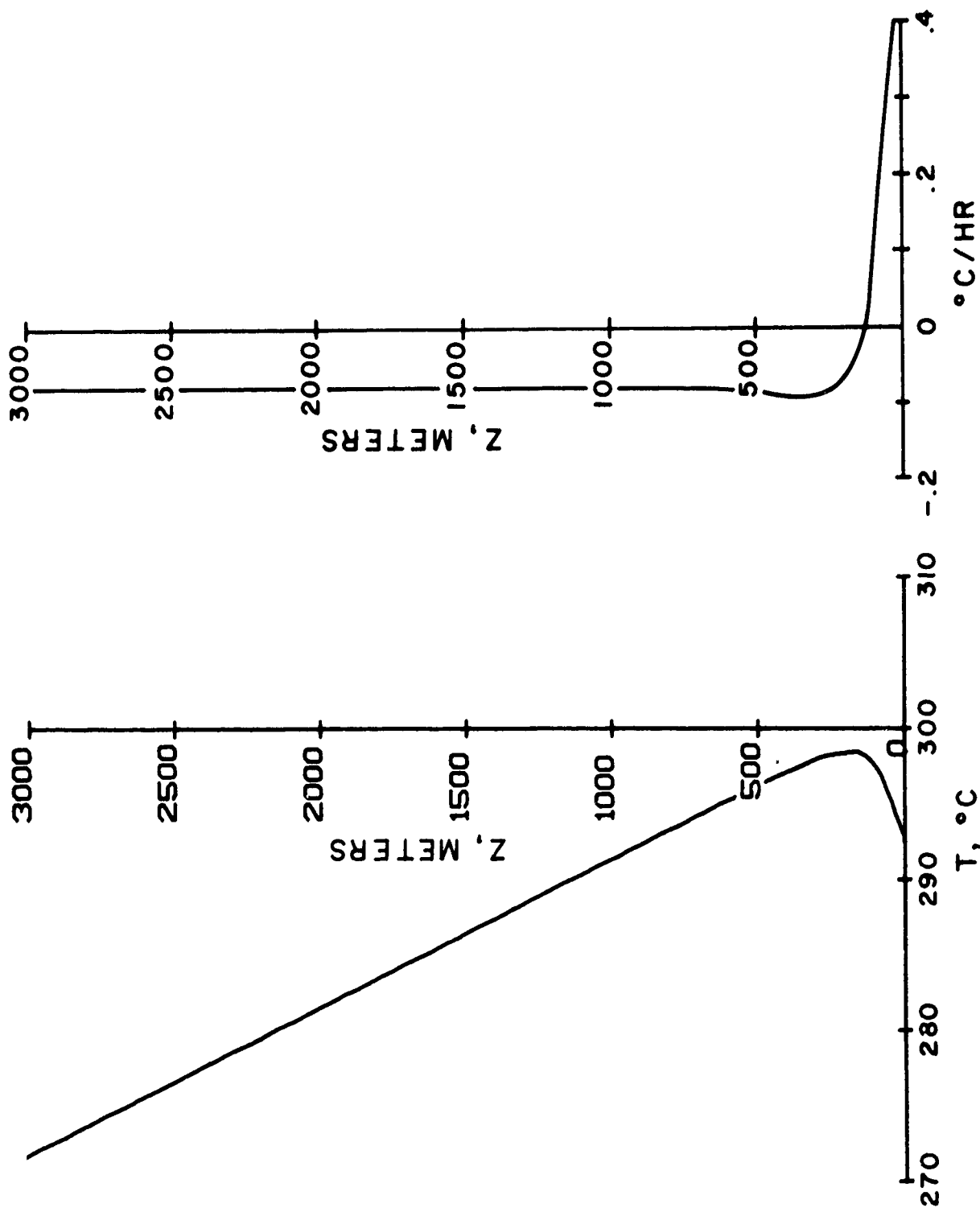
19

Figure 5-a. Absolute temperature and radiation flux divergence as a function of height at selected times during the day: 0600 local time.
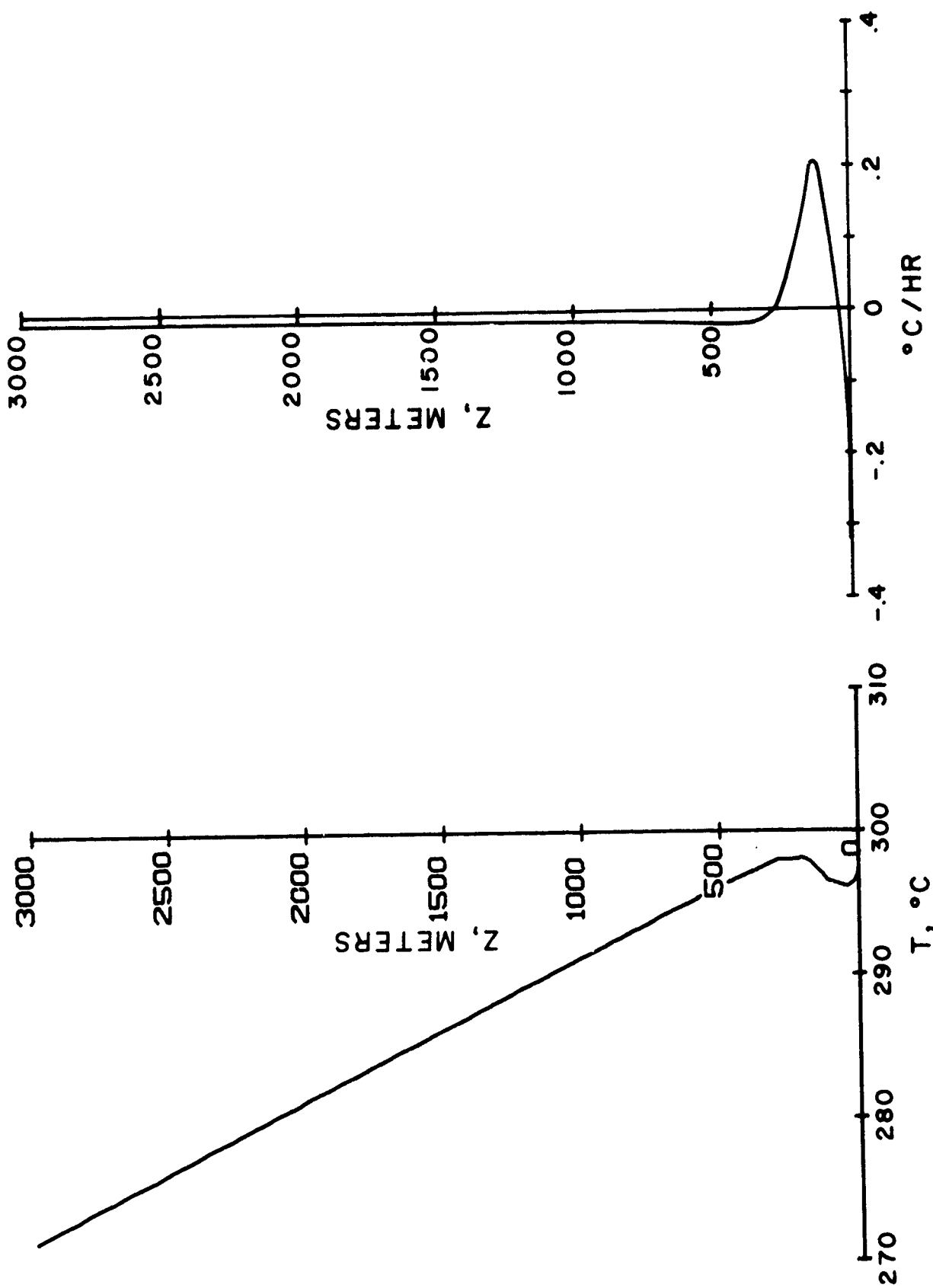
Figure 5-b. Absolute temperature and radiation flux divergence as a function of height at selected times during the day: 0900 local time.
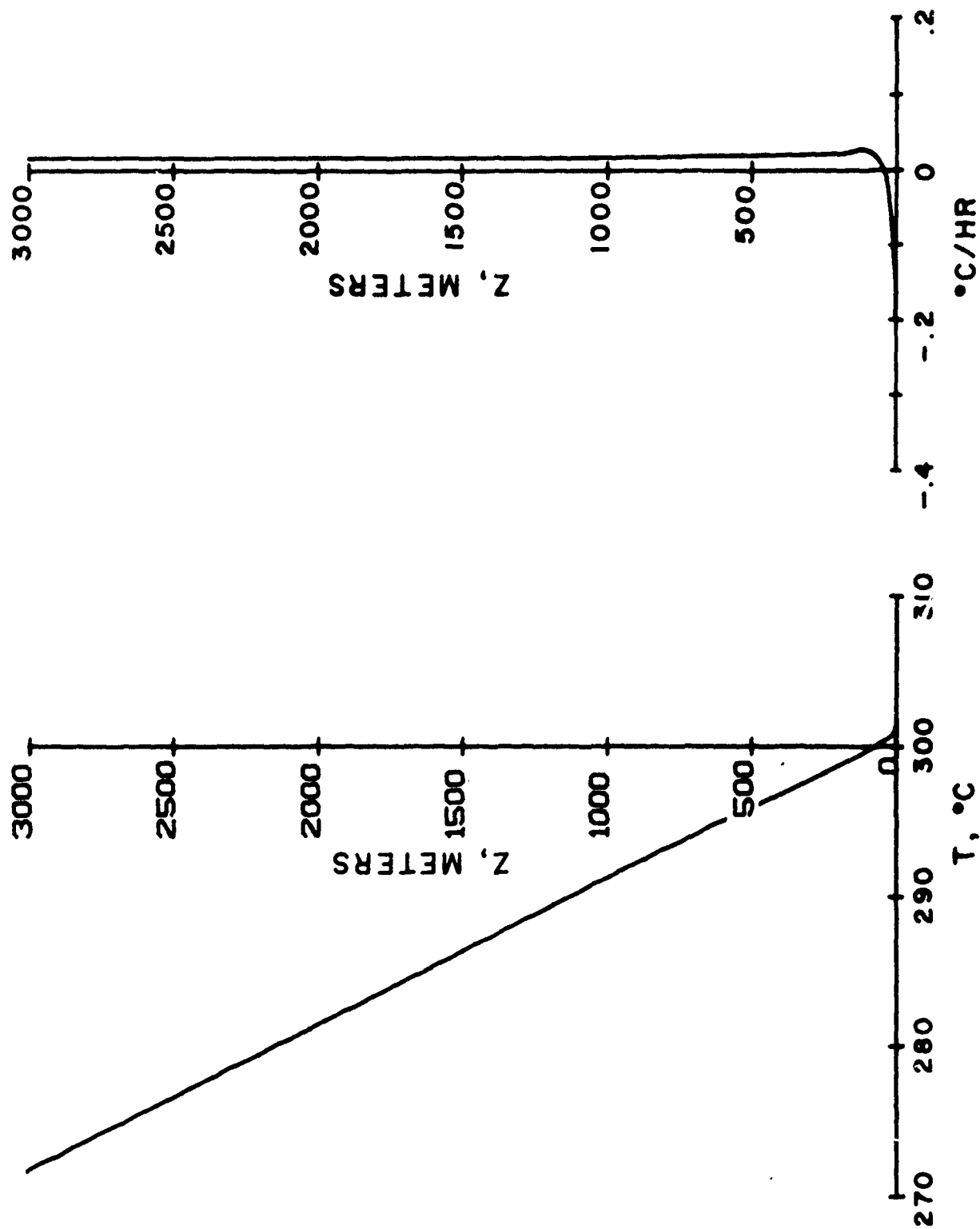
21

Figure 5-c. Absolute temperature and radiation flux divergence as a function of height at selected times during the day: 1030 local time.
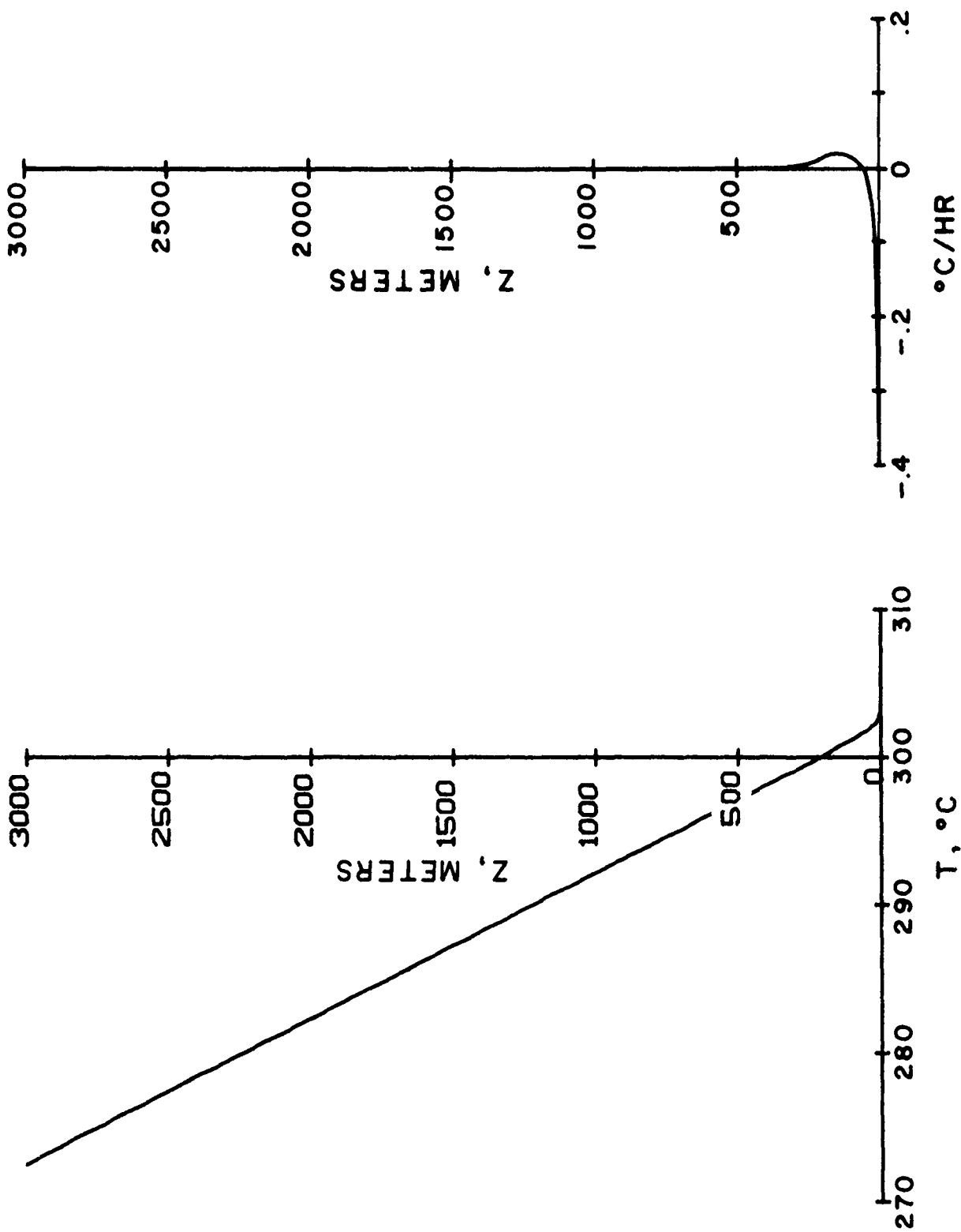
22

Figure 5-d. Absolute temperature and radiation flux divergence as a function of height at selected times during the day: 1424 local time.
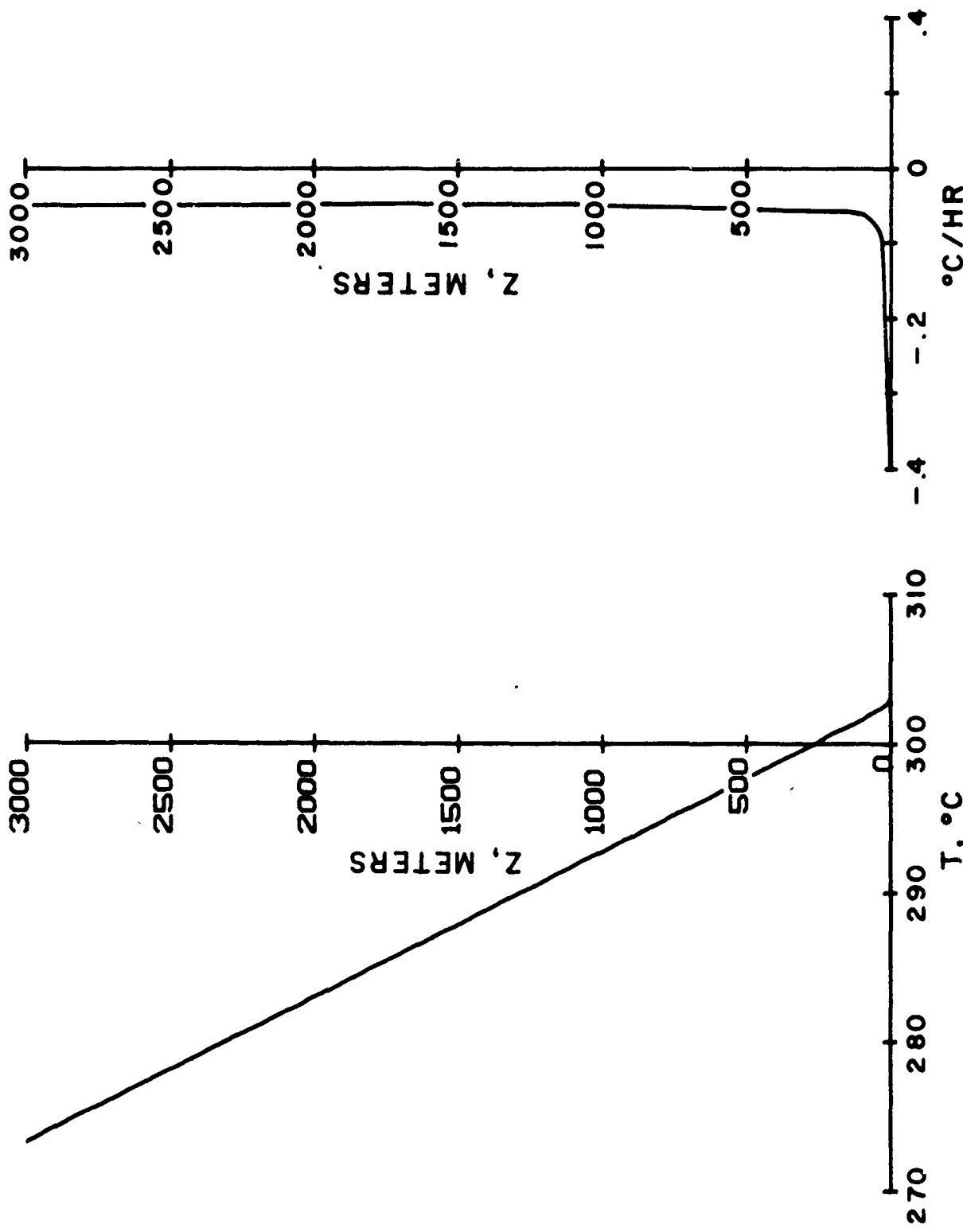
Figure 5-e. Absolute temperature and radiation flux divergence as a function of height at selected times during the day: 1900 local time.
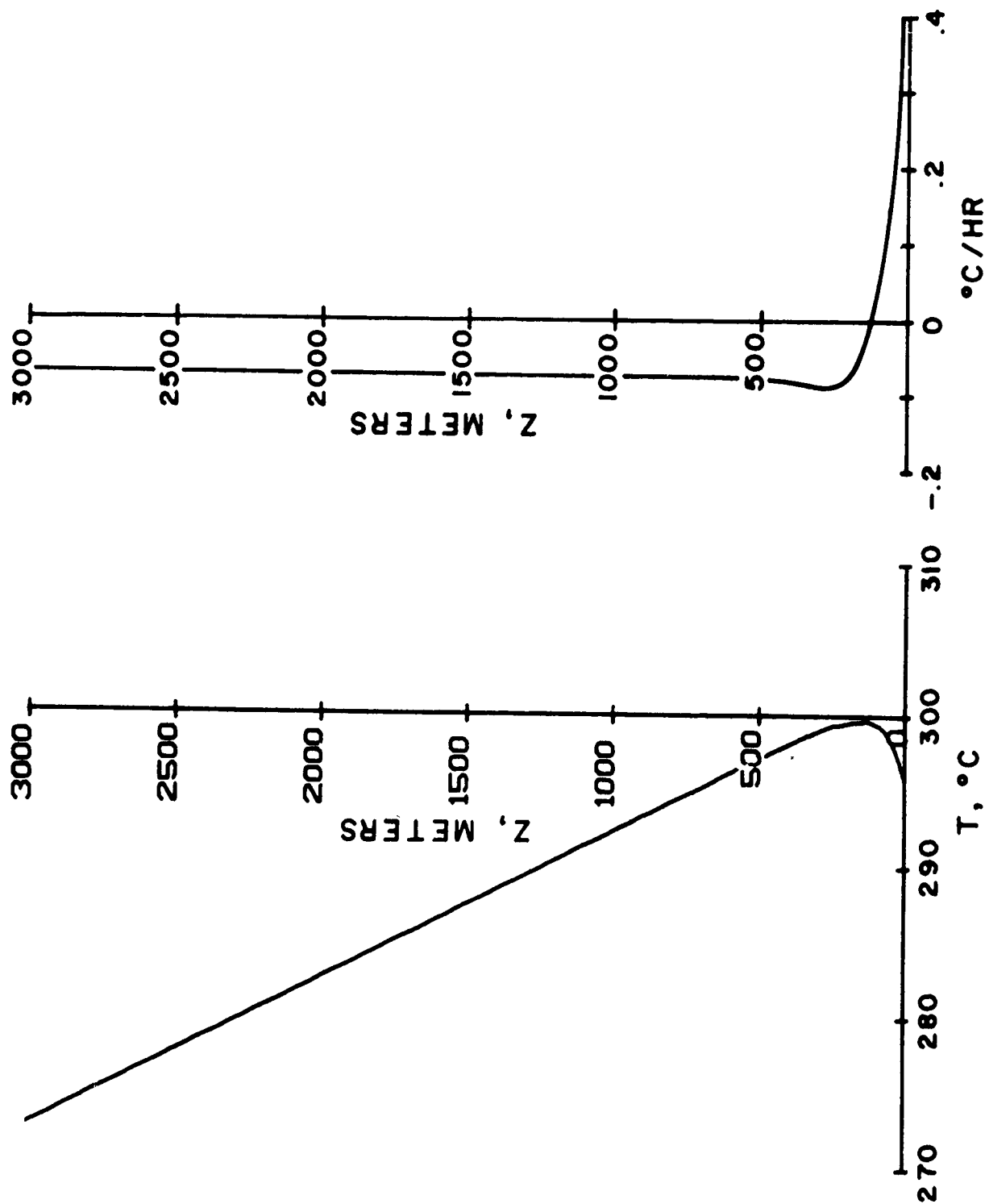
Figure 5-f. Absolute temperature and radiation flux divergence as a function of height at selected times during the day: 0200 local time.

detailed radiative prediction. Thus, with detailed radiative prediction the maximum turbulent squared velocity fluctuations are as high as 6.2 m^2/sec^2, occur slightly earlier in the day (2 p.m.), and at somewhat higher altitude (900 meters) than with previous calculations (4.8 m^2/sec^2 maximum at about 4 p.m. at about 600 meters).

The fact that the nocturnal turbulence is not quite as strongly damped, reduces the maximum angle at which the surface wind can deviate from geostrophic (36° as opposed to 42°) and locates the occurrence of the minimum angle deviation earlier in the day (about 10 a.m. rather than noon time), Fig. 6. These results, obtained with detailed radiation predictions, are closer to the wind angle data of Hoxit (Ref. 15) than those obtained with the simple radiation loss term.

3.2 Diurnal Variation in the Marine Atmospheric Boundary Layer

For a sample calculation of the one-dimensional, unsteady boundary layer over the ocean, we will assume that the ocean's surface temperature is constant at 22°C, that the geostrophic wind is constant at 10 m/sec, that the upper level humidity ratio is constant at 2.5×10^{-3} , and that the upper level potential temperature gradient is 0.006°C/m. The only diurnal variation introduced is in the solar, short-wave radiation, which goes through a 12-hour sine wave from 0600 local time to 1800.

Due to the large temperature gradients which occur at cloud tops, this calculation has also been run with the quasi-equilibrium assumption outlined earlier, so that time steps are not limited to a fraction of the local Brunt-Väisälä period. The run is started with a mixed layer depth of 500 meters and runs through three day's of simulated time. Although the results show a clear diurnal cycle, they have a substantially larger nonperiodic drift than is evident in the previous results over land. Figure 7 gives the contours of constant q^2 as a function of time and altitude for
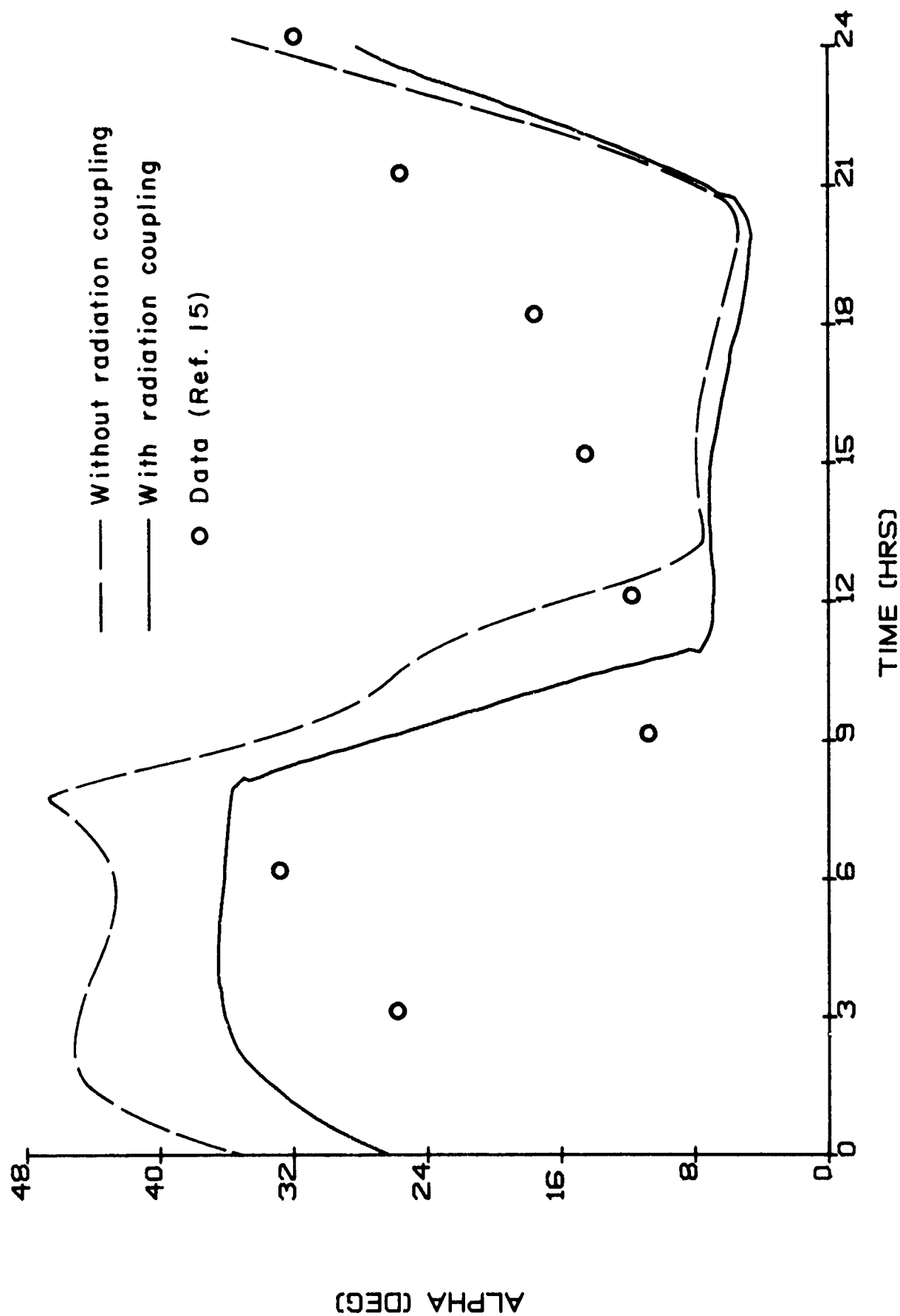
26

Figure 6. Angle between surface wind and geostrophic wind as a function of time for a typical midwestern summer day, computed with and without radiation coupling.
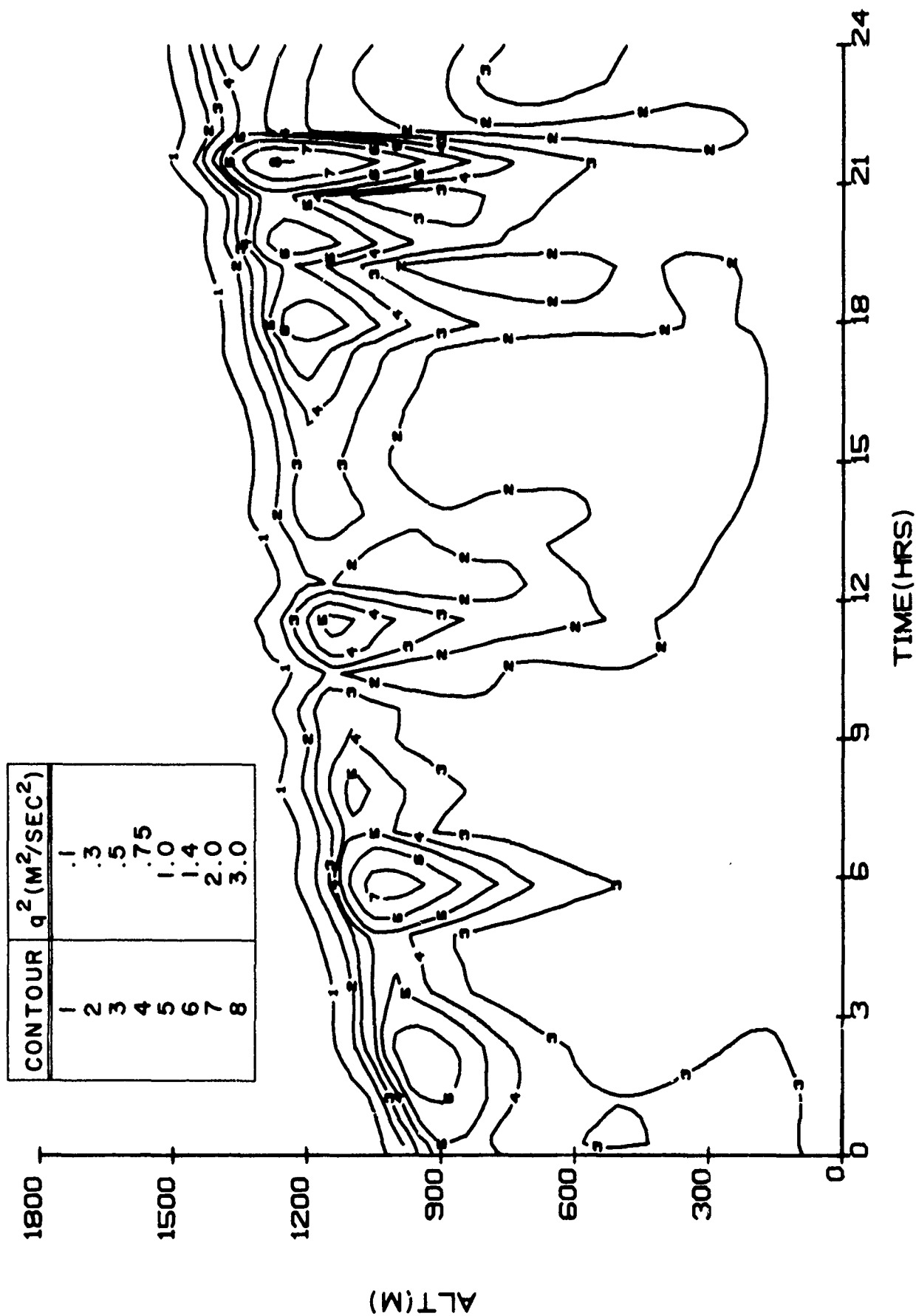
27

Figure 7. Turbulent kinetic energy as a function of time of day and altitude for a marine day. $U_g = 10$ m/sec, $f = 10^{-4}$ sec^{-1}, $T_S = 295°$K, $[\partial\theta/\partial z]_\infty = 6°$C/km. Second day of simulation shown.

day two of the simulation The growth in mixed layer depth evident throughout this day continues for the full three-day simulation The diurnal cycle shows up most clearly in the lower half of the mixed layer, where the turbulence is larger during the nocturnal hours than during the afternoon hours, This is the opposite condition from that generally found over land (see Fig. 6). The surface conditions are unstable (negative Monin-Obukhov length) throughout the day, but more unstable at night due to a combination of constant surface temperature and relatively strong, long-wavelength cooling. The instability is reduced in the afternoon by the solar heating of the air,

Figure 8 shows the contours of liquid water content. The maximum liquid water content occurs at the top of the mixed layer where there is a thin layer of scattered clouds throughout the day. The maximum thickness of clouds occurs near midnight, but is a relatively weak maximum compared with the rest of the day More than half of the cloudiness predicted in this calculation is of the scattered variety, that is, the turbulent fluctuations in H and T permit the coexistence at the same altitude of clouds and clear sky, Our program predicts the ensemble average of this condition, so that it is fair to think of the contours in Fig. 8 as what would be obtained if the average over a relatively large expanse of ocean were taken. The fluctuations in H and T play a particularly significant role in the top edge of the cloud,

Mixing ratio isolines of total water content, vapor plus liquid are shown in Fig. 9, As expected, there is a sharp drop-off in $\bar{H}$ at the top of the mixed layer, The fact that water vapor is continually fed into the boundary layer at the surface is the prime reason for the continued growth of the mixed layer. There is no mechanism for withdrawing water from the boundary layer in the current model, In the real atmosphere this is provided generally by advection to regions of lower humidity or by precipitation,

TIME(HRS)

ALT(M)

1500
1200
900
600
300

0   3   6   9   12   15   18   21   24

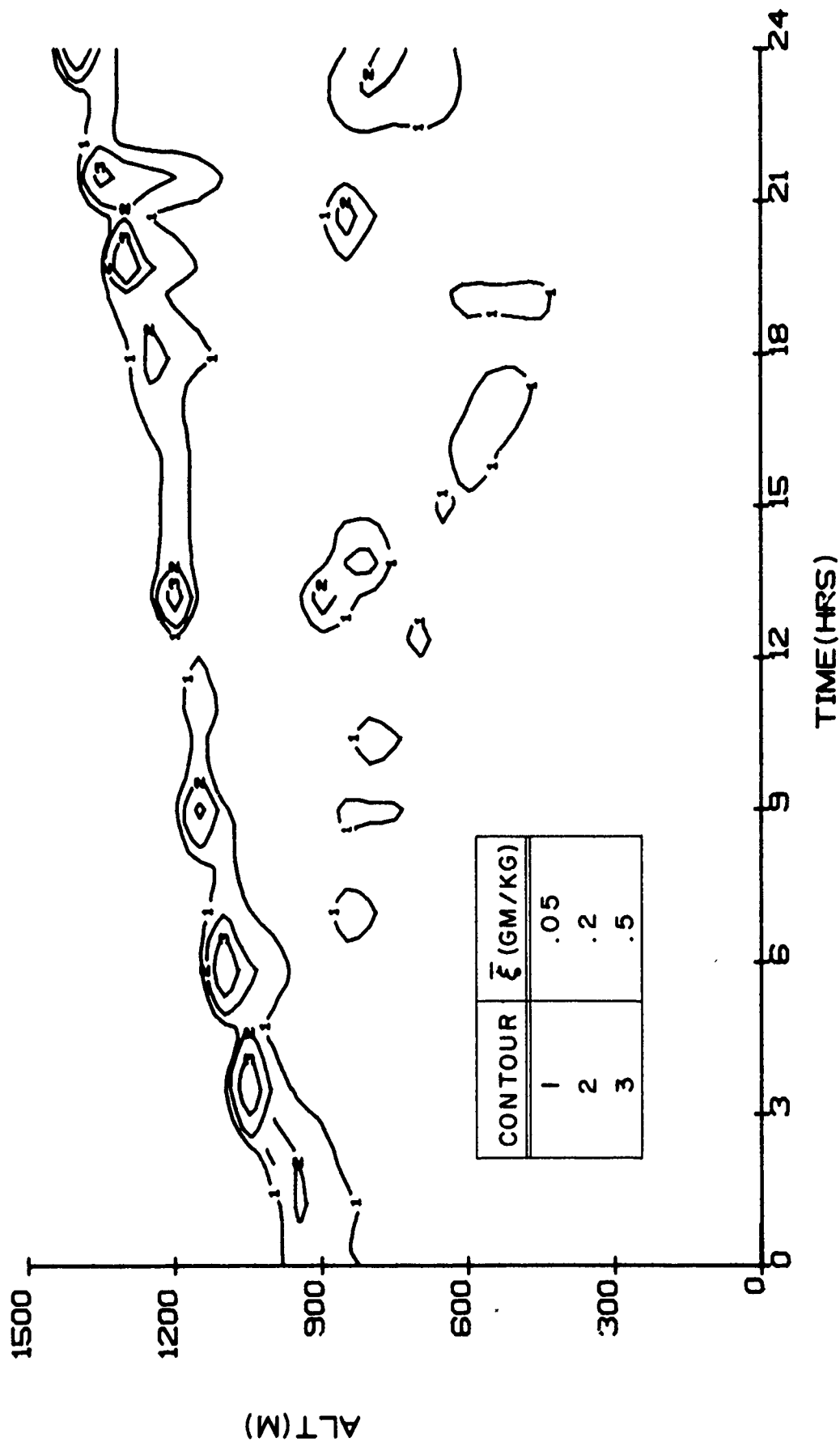| CONTOUR	$\bar{\xi}$ (GM/KG)
1	.05
2	.2
3	.5

Figure 8. Liquid water content as a function of time of day and altitude for the conditions of Figure 7.
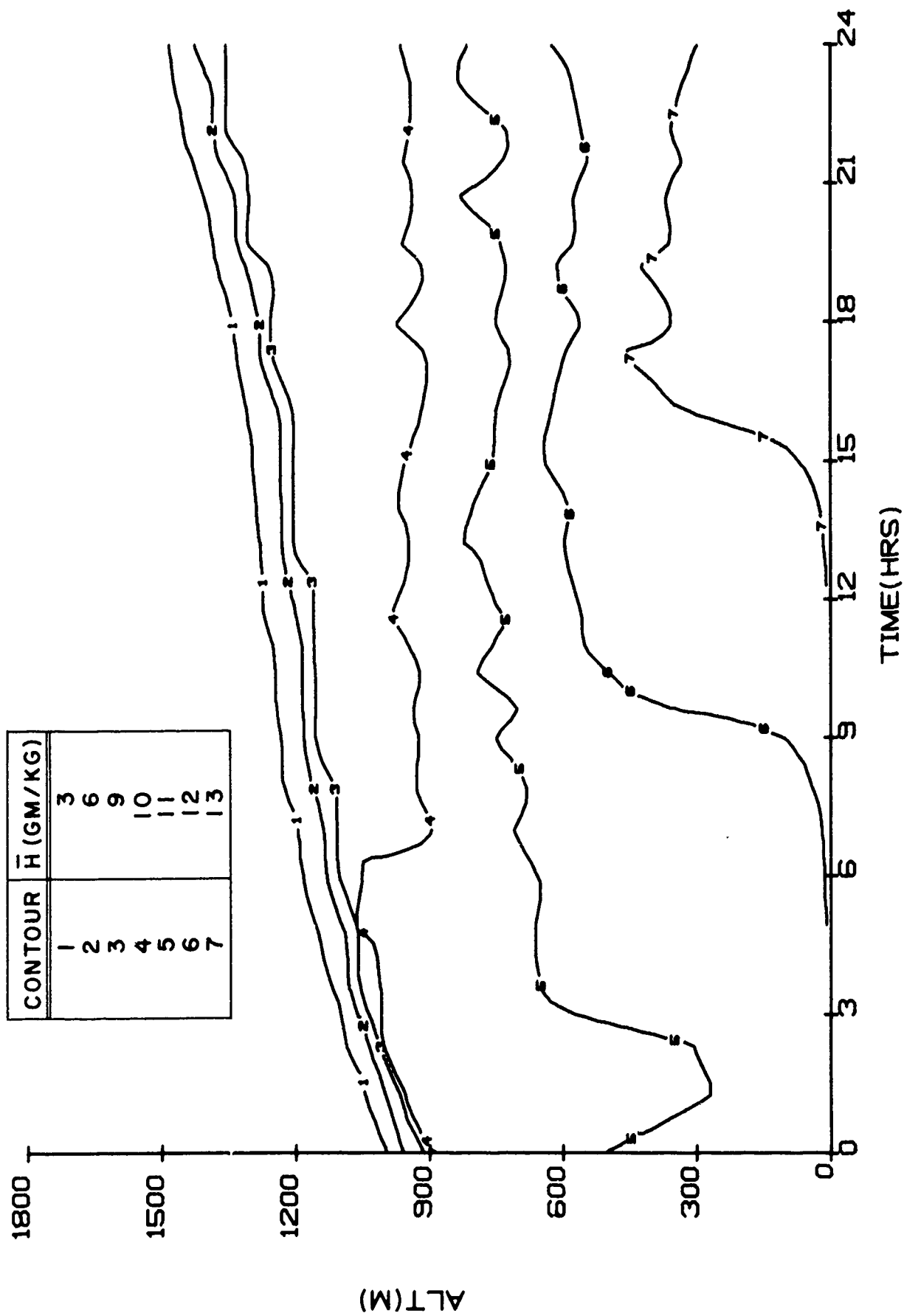
30

Figure 9. Humidity mixing ratio as a function of time of day and altitude for the conditions of Figure 7.

31

The contours of constant θ_v are shown in Fig. 10. The temperature gradient at the top of the mixed layer is accentuated by the strong radiational cooling of the cloud tops which occur here. Even when solar radiation is at its peak, the top of the clouds are cooled by long-wave radiation. This is evident in Fig. 11 which shows contours of constant radiation flux divergence. The cloud top cooling is sufficiently strong to induce a strongly unstable temperature gradient in the upper layer of the cloud. This leads to convectively produced turbulence which erases the temperature gradient as the mixed layer height is forced to grow. This causes the mixed layer to grow by a series of steps as evident in Fig. 10.

The wind component contours in Figs. 12 and 13 complete the description of the mean flow variables in the boundary layer. The upper part of the mixed layer has slightly supergeostrophic values of U. Values of V are relatively small throughout the day.

TIME(HRS)

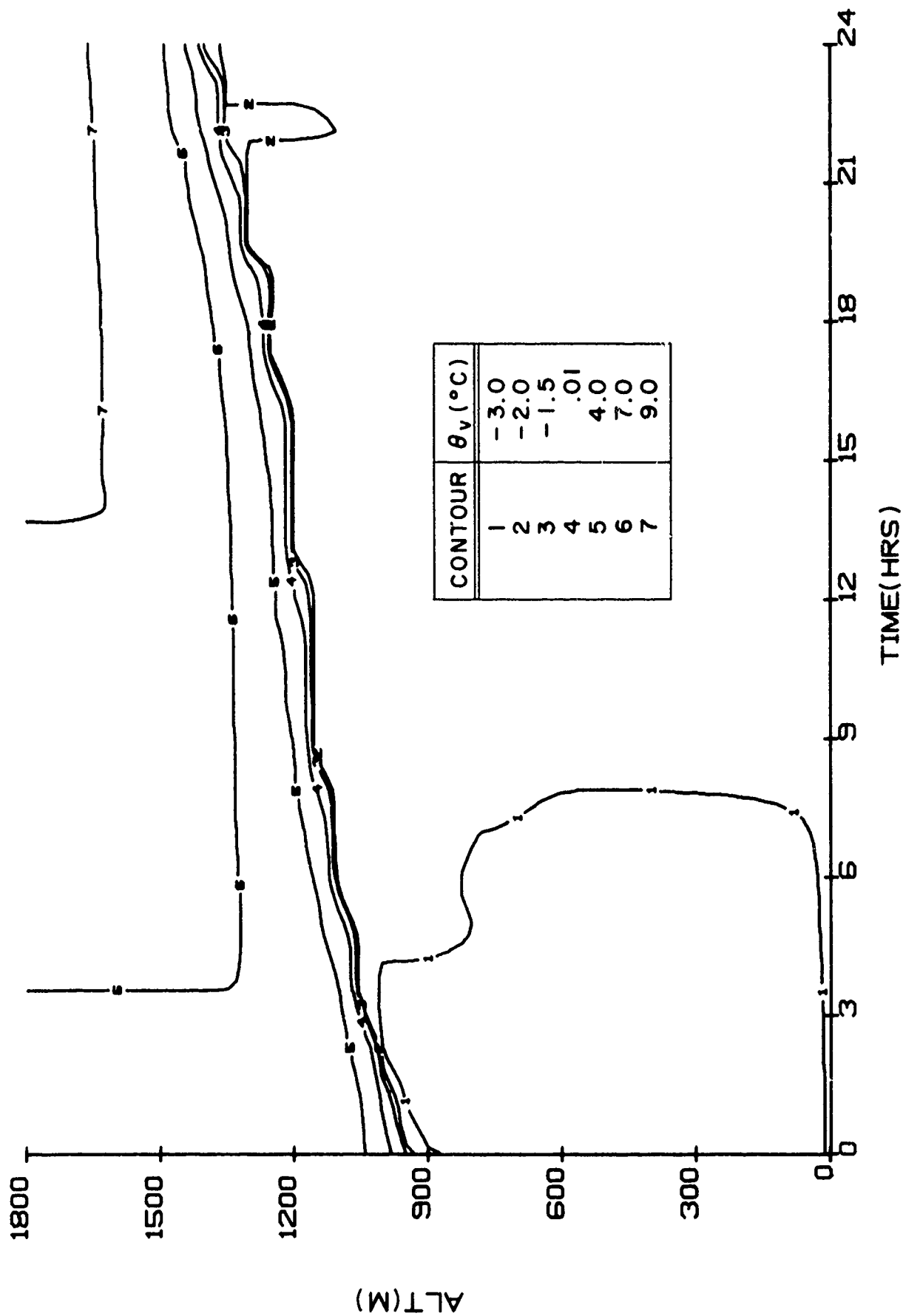| CONTOUR	θ_v(°C)
1	-3.0
2	-2.0
3	-1.5
4	.01
5	4.0
6	7.0
7	9.0

Figure 10. Virtual potential temperature as a function of time of day and altitude for the conditions of Figure 7.
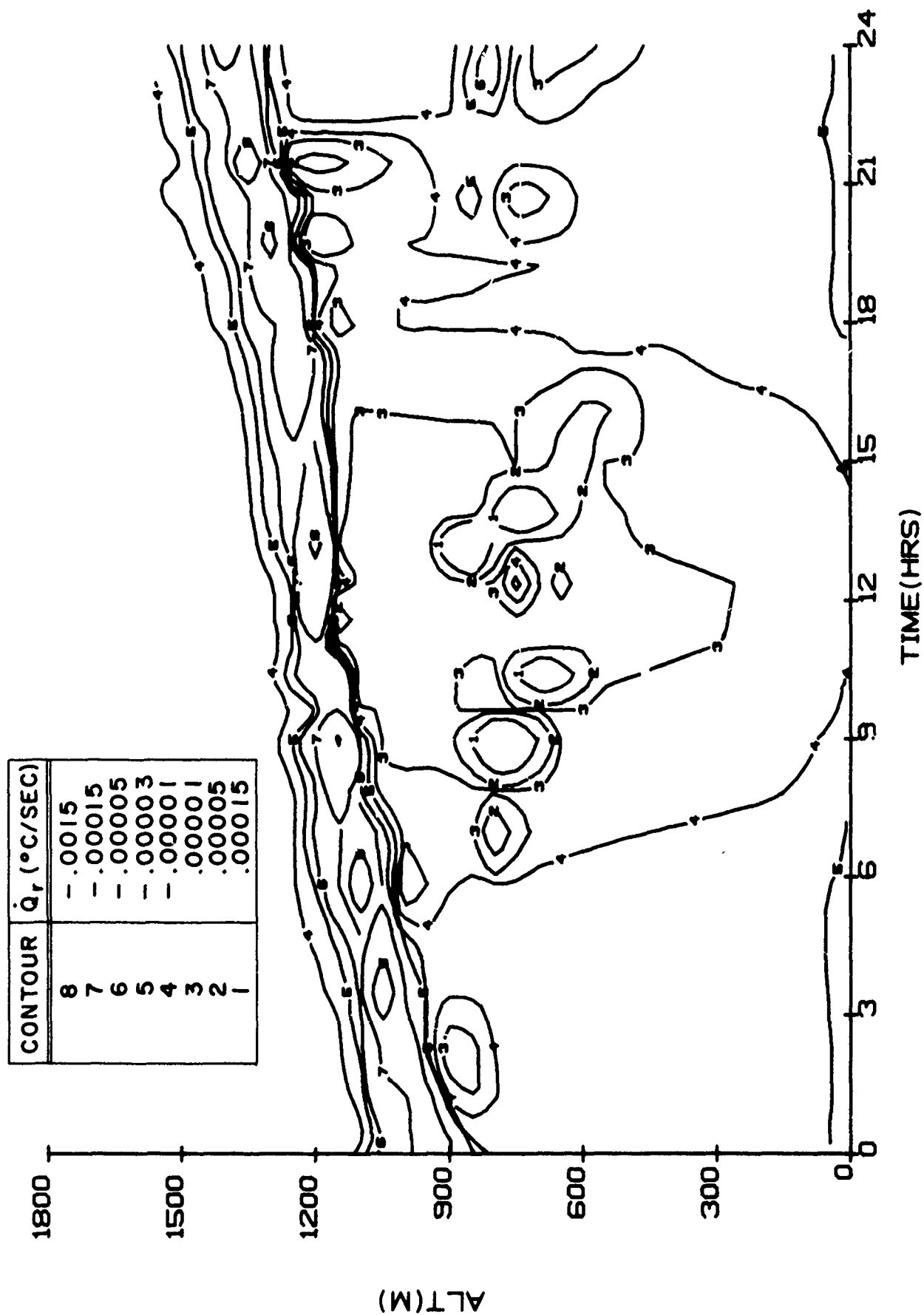
Figure 11. Radiative flux divergence as a function of time of day and altitude for the conditions of Figure 7.

CONTOUR	U (M/SEC)
1	8.0
2	9.0
3	9.5
4	10.0
5	10.1
6	10.2
7	10.4
8	10.5

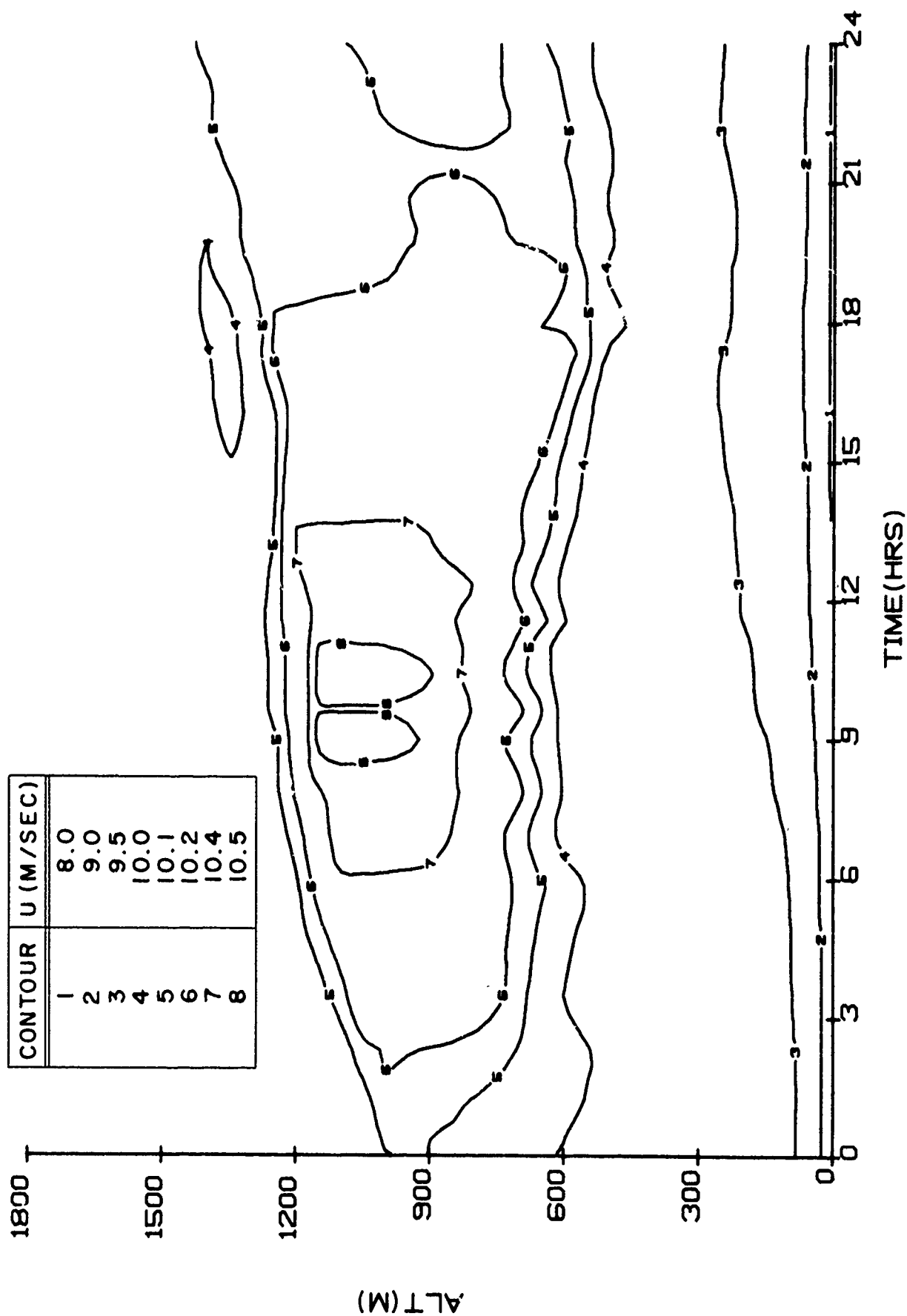Figure 12. Geostrophic component of the mean wind as a function of time of day and altitude for the conditions of Figure 7.
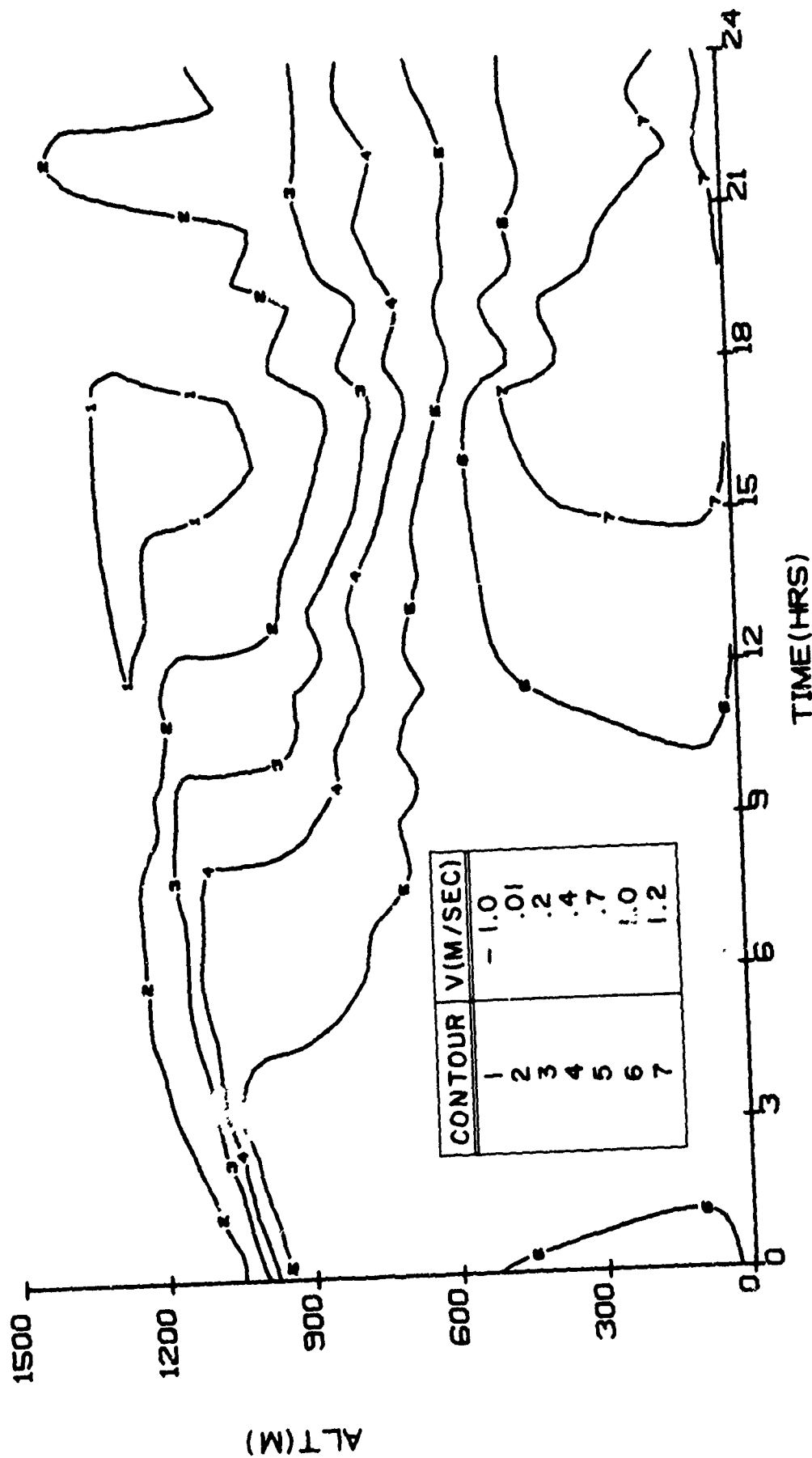
35

Figure 13. Component of the mean wind normal to the geostrophic wind as a function of time of day and altitude for the conditions of Figure 7.

CONTOUR	V(M/SEC)
1	-1.0
2	.01
3	.2
4	.4
5	.7
6	1.0
7	1.2

TIME(HRS)

ALT(M)

36

IV CONCLUSIONS AND RECOMMENDATIONS

Sample calculations show that the two major modifications to A.R.A.P.'s marine boundary layer code during the past year yield reasonable physical results. The increase in the dimensions of the program was used to make sample calculations of the sea-breeze circulation. The coupled thermal radiation model was used to make sample calculations of the typical diurnal variations in the boundary layer over both land and water. The physical characters of all of these results appear to agree, at least qualitatively, with observations.

To increase the confidence level in our model, it will be necessary to do more quantitative verification calculations. Two ways we believe this could be done over the coming year are: (1) to select a few well measured cases from the GATE (Global Atmospheric Research Program - Atlantic Tropical Experiment) data file and make detailed comparisons between our model predictions and field observations; and (2) to compare our model results with other sophisticated turbulent model calculations such as have been performed in Refs. 16 and 17 using a subgrid scale closure scheme while attempting to compute all of the three-dimensional, unsteady turbulent eddies above a given size. These verification comparisons should permit a detailed assessment of the accuracy of our model.

Currently, only the one-dimensional program has the full capability of permitting condensation and a coupled radiation code. This capability should be incorporated into the two-dimensional program. This extension will give the program the capability of computing coastal fog conditions.

Other modifications to the program which it appears desirable to consider are the removal of the hydrostatic assumption from the two-dimensional, unsteady program to permit features such as the sea-breeze gust front to be better defined; the incorporation of the capability of computing the flow over a step change

in elevation as occurs at many shoreline locations, and the incorporation of the capability of predicting the turbulent diffusion of aerosols of a known composition.

The ultimate goal of our program is to provide the Navy with detailed predictions of the low-level distributions of pertinent atmospheric variables. With the accomplishment of the above tasks, in particular the detailed verification comparisons, the program should be ready to test by investigating distributions at some specific sites and at given times of interest to the Navy.

V. REFERENCES

1. Donaldson, Coleman duP.: Construction of a Dynamic Model of the Production of Atmospheric Turbulence and the Dispersal of Atmospheric Pollutants. In Workshop on Micrometeorology, American Meteorological Society, Science Press, 1973, pp. 313-392.

2. Lewellen, W.S. and Teske, Milton E.: Turbulence Modeling and its Application to Atmospheric Diffusion, Part I: Recent Program Development, Verification, and Application. Part II: Critical Review of the Use of Invariant Modeling. EPA-600/4-75-016a&b, August 1975.

3. Lewellen, W.S. and Teske, M.E.: Predictions of the Monin-Obukhov Similarity Functions from an Invariant Model of Turbulence. J. Atmos. Sciences 30, 1973, pp. 1340-1345.

4. Lewellen, W.S., Teske, M.E. and Donaldson, Coleman duP.: Turbulence Model of Diurnal Variations in the Planetary Boundary Layer. Proc. 1974 Heat Transfer and Fluid Mechanics Institute (L.R. Davis & R.E. Wilson, eds.), Stanford Univ. Press, 1974, pp. 301-319.

5. Lewellen, W.S., Teske, M.E., and Donaldson, Coleman duP.: Examples of Variable Density Flows Computed by a Second-Order Closure Description of Turbulence. AIAA J. 14, 3, March 1976, pp. 382-387.

6. Lewellen, W.S. and Teske, M.E.: Second-Order Closure Modeling of Diffusion in the Atmospheric Boundary Layer. Boundary Layer Meteor. J. 10, 1976, pp. 69-90.

7. Lewellen, W.S. and Teske, M.E.: Development of a Low-Level Atmospheric Turbulence Model for Marine Environments. A.R.A.P. Report No. 255, September 1975.

8. Verma, S.B. and Cermak, J.E.: Mass Transfer from Aerodynamically Rough Surfaces. Int. J. Heat Mass Transfer 17, 5, 1974, pp. 567-579.

9. Wu, Jin: Froude Number Scaling of Wind-Stress Coefficients. J. Atmos. Sciences 26, 3, 1969, pp. 408-413.

10. Wyngaard, J.C., Izumi, Y., and Collins, S.A.: Behavior of the Refractive-Index-Structure Parameter Near the Ground. J. Optical Soc. of America 61, 12, 1971, pp. 1646-1650.

11   Augstein, E., Schmidt, H. and Ostapoff, F.:   The Vertical
      Structure of the Atmospheric Planetary Boundary Layer in
      the Undisturbed Trade Winds Over the Atlantic. Boundary
      Layer Meteor. $\underline{6}$, 1974, pp. 129-150.

12.   Swarztrauber, P. and Sweet, R.:   Efficient FORTRAN Sub-
      programs for the Solution of Elliptic Partial Differential
      Equations. NCAR-TN/IA-109, 1975.

13.   Lyons, W.A.:   Turbulent Diffusion and Pollutant Transport
      in Shoreline Environments. Lecture on Air Pollution and
      Environmental Impact Analyses, AMS, 1975, pp. 136-208.

14.   Wyngaard, J.C.:   Notes on Surface Layer Turbulence. Work-
      shop on Micrometeorology, American Meteorological Society
      Boston, 1973.

15.   Hoxit, L.R.:   Diurnal Variations in Planetary Boundary Layer
      Winds Over Land. Boundary Layer Meteorology, Vol. 8, 1975,
      pp. 21-38.

16.   Sommeria, G.:   Three-Dimensional Simulation of Turbulent
      Processes in an Undisturbed Tradewind Boundary Layer. J.
      Atmos. Sci. $\underline{33}$, Feb. 1976, pp. 216-241.

17.   Sommeria, G.:   Direct Comparison of Three-Dimensional
      Numerical Simulation to Actual Data in the Tradewind
      Boundary Layer. Presented at the Tenth Technical Conf.
      on Hurricanes and Tropical Meteorology of the American
      Meteorological Society, July 6-9, 1976, Charlottesville,
      Va.

APPENDIX A

RADIANT HEAT TRANSFER PREDICTION
IN CLEAR, CLOUDY, AND TURBID
ATMOSPHERIC BOUNDARY LAYERS

D. A. Oliver

I. INTRODUCTION

A description of the principal atmospheric radiation effects in the planetary boundary layer has been developed for incorporation in the A.R.A.P. atmospheric boundary layer fluid mechanic models. This radiation model includes all important radiation effects in the lower atmosphere to at least a representative approximation. Certain radiative processes, however, are not treated in refined detail (notably, scattering (in contrast to absorption) of direct solar radiation by clouds and aerosols). The radiation model is for the average one-dimensional radiation field; hence, horizontal gradients and structure are not described except in an average sense.

At present, the statistical coupling of the radiation and fluid fields is not considered. In principle, the turbulent kinetic energy destruction which occurs at the high wave number end of the energy cascade could be influenced by radiative transport. Such effects have been examined in stellar atmospheres while very limited fluid turbulence interaction with a fluctuating radiation field has been examined by Goody.[1]

The present radiation model is directed to the interaction with the mean fluid equations where the radiation cooling/heating enters directly into the mean energy flow. The effect on the turbulence can, however, be quite profound. Local radiative cooling or heating can alter the local temperature profile thereby overturning the stability of the fluid or rendering it stable. Hence, atmospheric radiation can have an important coupling with atmospheric turbulence through the mean flow and mean radiation fields. The present model is constructed to reveal this interaction.

II. SUMMARY OF THE RADIATION MODEL

The present radiation model consists of two principal components: (1) the representation of direct solar heating concentrated in the 0.7μ to 2μ wavelength range, and (2) the

representation of terrestial thermal radiation concentrated in the 2μ to 40μ wavelength range. These two fields are, in effect, treated separately in their interactions with matter with respect to absorption, emission, and scattering. They are then combined to yield the net heating or cooling of the fluid. The model thus provides for:

1. Calculation of radiant fluxes and heating due to direct solar radiation including the effects of:
   a. atmospheric molecular absorption by CO_2
   b. atmospheric molecular absorption by H_2O vapor
   c. atmospheric absorption by aerosols
   d. absorption by condensed liquid water in clouds or fog
   e. reflectance from the surface over which the boundary layer flows

2. Calculation of radiant fluxes and heating due to terrestial (long wavelength) thermal radiation including the effects of:
   a. atmospheric molecular absorption by CO_2
   b. atmospheric molecular absorption by H_2O vapor
   c. absorption by condensed liquid water in fogs and clouds

3. Parameterization of the upper atmosphere radiation properties. Since the model is primarily intended for use in the lower atmospheric boundary layer (elevations of 3 km or lower), the radiation interaction of the upper atmosphere with the boundary layer requires specification. These are parameterized in the present model by the specification of three average upper atmosphere properties:
   a. average cloudiness (condensed liquid water density) of the upper atmosphere
   b. average humidity of the upper atmosphere (mass fraction of water vapor)
   c. average turbidity of the upper atmosphere (mass fraction of aerosols)

A-2

III. RADIATION VARIABLES AND THE RADIATIVE TRANSPORT EQUATIONS

The present radiation model is constructed to describe the frequency and angular averaged radiative intensity and fluxes. Further, all variables are assumed to be a function of a single spatial coordinate, the elevation z . The fundamental radiation variables for either the direct solar radiation or the long wavelength radiation fields are as follows:

F^+ Frequency and angular integrated upward directed radiant flux

F^- Frequency and angular integrated downward directed radiant flux

q^r Radiant heat flux

S Radiant source function

$F^+(z_o)$ Upward flux at the base of the boundary layer $z = z_o$

$F^-(H)$ Downward directed flux at the edge of the upper atmosphere $z = H$

$\sum_\odot$ Downward directed direct solar radiation at the edge of the upper atmosphere

$\tau(z_1,z_2)$ Transmission function for a given radiation field (either direct solar or long wavelength) between levels z_1 and z_2

The fluxes $F^+(z)$, $F^-(z)$ are the basic radiative variables and are governed by the upward and downward transport equations in integral form [Goody[2], Ellingson[3], Atwater[4], Rodgers and Walshaw[5]]

$$F^+(z) = F^+(z_o)\tau(z_o,z) + S(z) - S(z_o)\tau(z_o,z)$$

$$-\int_{z_o}^{z} \tau(z',z) \frac{\partial S}{\partial z'} dz' \qquad (1a)$$

A-3

$$F^-(z) = F^-(H)\tau(H,z) + S(z) - S(H)\tau(H,z)$$

$$- \int_H^z \tau(z',z) \frac{\partial S}{\partial z'} dz' \qquad (1b)$$

Given the source function $S(z)$, transmission function $\tau(z_1,z_2)$ and the boundary values $F^+(z_o)$ and $F^-(H)$, Eqs. (1) uniquely determine the flux fields $F^+(z), F^-(z)$. The radiative heat flux is then

$$q^r(z) = F^+(z) - F^-(z) \qquad (2)$$

while the radiative heating/cooling rate is given by

$$-\nabla \cdot \vec{q}^r = - \frac{d}{dz}[F^+(z) - F^-(z)] \qquad (3)$$

The absorption, scattering, and emissive properties of the atmosphere are embedded in the source function $S(z)$ and transmission function $\tau(z_1,z_2)$. These functions are different for the long wavelength radiation field and the short wavelength radiation field. So also are the boundary conditions $F^+(z_o)$ and $F^-(H)$.

We note that alternative, more flexible formulations and solution representations of the radiative transport equations exist [e.g., Marchuk[6]]. However, molecular absorption is a principal atmospheric absorption mechanism and the spectra are therefore discrete rather than continous. Line profile distortion (variation of absorption over the line) has a profound effect on atmospheric radiation absorption and cannot be readily described by schemes such as those of Marchuk[6]. Neglect of line profile distortion for molecular absorbers like CO_2 and water vapor can lead to errors of the order of 50% in absorption prediction. The integral formulation given above (though less flexible with respect to boundary conditions) can readily incorporate the line profile distortion characteristic of molecular absorbers in the transmission function.

IV. TERRESTIAL RADIATION

We now discuss the boundary values $(F^+(z_o), F^-(H))$, source function $(S(z))$, and transmission function $\tau(z_1, z_2)$ appropriate for terrestial radiation in the lower atmosphere. Although there is evidence that strong nonequilibrium effects exist in the upper rarefied atmosphere, Kirchhoff's law holds quite well in the boundary layer region and it is permissible to set the radiant source function equal to the Planck function:

$$S(z) = B(z) \equiv \sigma T^4(z) \qquad (4)$$

(σ is the Stephan-Boltzmann Constant).

Appropriate vlaues for the boundary conditions are

$$F^+(z_o) = B_o \qquad (5)$$

$$F^-(H) = \varepsilon B(H) \qquad (6)$$

In the above, B_o is a boundary Planck function which in general is equal to $B(z_o)$; however, a discontinuity between surface and lower atmospheric temperature is permitted for certain kinds of modelling in which the analyst need not specify $B_o = B(z_o)$.

The parameter ε is the upper atmosphere emissivity for downward radiation. If $z = H$ lies outside the atmosphere and no thermal radiation is incident upon the earth, a rigorous condition is $\varepsilon = 0$. In practice, it is found that a value of $\varepsilon \sim 0.1 - 0.15$ applied at the "edge" of the upper atmosphere ($p \sim 10$ mb) gives reasonable agreement with experimental measurements of $F^-(z)$ [Ellingson[7]].

The transmission function $\tau(z_1, z_2)$ describes the atmospheric interaction with the radiation field. For the three components which interact, let us denote by subscripts $i = 1, 2, 3$ the following.

$$\rho_1(z) = \text{mass density of } H_2O \text{ vapor}$$

$$\rho_2(z) = \text{mass density of } CO_2$$

$$\rho_3(z) = \text{mass density of } H_2O \text{ liquid}$$

The transmission function $\tau(z_1, z_2)$ can then be considered to be a function of the mass areal densities m_i in the interval (z_1, z_2) as

$$\tau(z_1, z_2) = \tau(m_1, m_2, m_3)$$

where the mass areal density for species i, m_i is defined as

$$m_i = \int_{z_1}^{z_2} \rho_i \, dz \qquad (7)$$

The transmission function for long wavelength radiation is modelled after that of Feigel'son[8]:

$$\tau(m_1, m_2, m_3) = T_3(m_3) \left\{ \sum_{k=1}^{3} a_k^{(1)} \exp\left(-\beta \alpha_k^{(1)} m_1\right) \right.$$
$$\left. + \prod_{n=2}^{3} \sum_{k=1}^{3} a_k^{(n)} \exp\left[-\beta \alpha_k^{(n)} m_{n-1}\right] \right\} \qquad (8)$$

The function $T_3(m_3)$ accounts for cloudiness:

$$T_3(m_3) = \exp\left[-\beta \alpha m_3\right] \qquad (9)$$

In the above transmission functions the coefficient β is the diffusivity factor which accounts for the fact that the terrestial radiation is diffuse rather than collimated [$\beta = 1.66$, Elsasser[9]]. The coefficients $a_k^{(n)}$, $\alpha_k^{(n)}$ have been computed by Feigel'son[10] [Table III.2.3, p. 83] to accurately match the summary of CO_2 and H_2O vapor laboratory measurement data compiled by Davis and Viezee[11]. For $m_1 < 10$ gm/cm^2 and $m_2 < 100$ gm/cm^2 the Feigel'son transmission function matches the data summary of Davis and Viezee within 5% for CO_2 and H_2O vapor.

The coefficient α in the transmission component T_3 accounts for the absorptive properties of liquid water. For long wavelength thermal radiation in the range from 2 to 40μ the absorptive characteristics of water droplets depend strongly upon their size. Hence, an accurate description of the absorption in a cloud

requires specification of the droplet size distribution within the cloud.

Feigel'son[12] and Gradus, et al.[13] have determined the effective absorption coefficient α for droplet radii distribution functions of the form

$$N(r) = N_o r^n e^{-ar}$$

where (n,a) are parameters characterizing the distribution. These parameters are in turn related to cloud type. Small values of n and a correspond to so-called "narrow" distributions, while large (n,a) correspond to "wide" distributions. Narrow distributions are characteristic of Ns , St , II , while wide distributions are characteristic of Sc , As . Clearly, wide distributions are clouds dominated by large droplets while narrow distributions are dominated by small droplets. Fogs or low-lying marine clouds would perhaps be more typical of the narrow distribution. These distribution functions are utilized with the spectral absorption cross sections of droplets of different radii tabulated by Herman[14] and Zel'manovich, et al.[15] to yield the total absorption coefficient α . The results of these detailed calculations for

$$\left.\begin{array}{l} n = 4.5 \\ a = 1.5\mu \\ r_{ave} = 4.5\mu \end{array}\right\} \quad \text{narrow distribution}$$

and

$$\left.\begin{array}{l} n = 2 \\ a = 0.4\mu \\ r_{ave} = 7.0\mu \end{array}\right\} \quad \text{wide distribution}$$

are

$$\alpha = \left\{\begin{array}{ll} 500 \text{ cm}^2/\text{gm} & \text{(wide)} \\ 1700 \text{ cm}^2/\text{gm} & \text{(narrow)} \end{array}\right.$$

A-7

The factor of 3 or more difference between these two absorption
coefficients points out clearly that accurate prediction of
radiation in a cloudy atmosphere requires a correlation between
cloud type (n, a, r_{ave}) and its local thermodynamic state $(\rho_1, \rho_3,$
Temperature), and perhaps its condensation history. Such detail
is not included in the present radiation model. Rather we treat
the absorption α as a cloud type parameter varying between 500
and 1700 cm^2/gm.

V. DIRECT SOLAR RADIATION

We now turn to the boundary values $[F^+(z_o), F^-(H)]$, source function $S(z)$ and transmission function $\tau(z_1, z_2)$ appropriate for direct solar radiation. The approximation that emission into the short wavelength spectrum is negligible is made so that for the direct solar radiation field we set

$$S(z) \equiv 0$$

The boundary values are set as

$$F^-(H) = \sum_{\odot}$$
$$F^+(z_o) = \Gamma F^-(z_o)$$

where Γ is the surface reflectance for direct solar radiation. The short wavelength transmission function formally depends upon four absorbing areal mass densities as

$$\tau(z_1, z_2) = \tau(m_1, m_2, m_3, m_4)$$

where $m_i (i = 1,2,3)$ are as defined in Eq. (7) and m_4 is the aerosol areal mass density defined in terms of the volumetric aerosol density ρ_4 as

$$m_4 = \int_{z_1}^{z_2} \rho_4 dz \qquad (10)$$

The short wavelength transmission function is then given by

$$\tau(m_1, m_2, m_3, m_4) = T_v(m_1) \cdot T_g(m_2) \cdot T_\ell(m_3) \cdot T_a(m_4) \qquad (11)$$

Band overlap between CO_2 and H_2O vapor can be neglected for the short wavelength radiation; hence, the total transmission function can be expressed as the product of the individual species transmission functions. Further, line profile distortion is important for the water vapor transmission function T_v so we represent it in the functional form

$$T_v(m_1) = 1 - a_v \sqrt{m_1} - \ln \left(1 + \frac{\sqrt{m_1}}{b_v}\right) \qquad (12)$$

which embraces the functional forms for strong and weak band absorption [Sivkov[16]].   The parameters a_v , b_v are selected as

$$a_v = 0.04$$

$$b_v = 15$$

when m_1 is in units of gm/cm^2. The water vapor transmission function, Eq. (12), with these parameter choices of a_v , b_v matches the data of Sivkov[17] and Manabe and Strickler[18] for $m_1 < 3 \ gm/cm^2$ within 5%.

The transmission functions for water vapor free air and liquid water are represented as

$$T_g(m_2) = \exp \left[-\beta \alpha_g m_2\right] \qquad (13)$$

$$T_\ell(m_3) = \exp \left[-\beta \alpha_\ell m_3\right] \qquad (14)$$

The absorption coefficient for the gaseous molecular components of clean water-free air is taken as

$$\alpha_g = 0.7 \times 10^{-4} \ cm^2/gm$$

which matches well the data of Sivkov[17], Manabe and Strickler[18], and Eltermann, et al.[19].

In the case of liquid water absorption of direct solar radiation, Feigel'son[20] notes that for wavelengths less than 2μ the absorption is not sensitive to droplet size. Further, the liquid water absorption spectrum is continuous so that the form Eq. (13) is quite accurate. Integrating the spectral liquid water absorption coefficient tabulated by Feigel'son[21] over the direct solar spectrum we find

$$\alpha_\ell = 13 \ cm^2/gm$$

Lastly, we consider the transmission $T_a(m_4)$ of the aerosol. Since the absorption by aerosol particles, like that of water droplets, can be considered to be continuous, the transmission function may be represented as

$$T_a(m_4) = \exp[-\alpha_a m_4] \qquad (15)$$

The absorption coefficient α_a is a sensitive function of the particle size distribution. As noted by Kondratyev[22], the particle size distribution of typical atmospheric aerosols varies significantly with height; hence, a detailed description of radiative interaction with the aerosol requires specification (or simultaneous prediction) of the particle size distribution function as well as the total aerosol mass density. In the event that ρ_4 and α_a are predictable or known in such detail, the form Eq. (15) is appropriate and useful.

In lieu of a detailed prediction procedure for ρ_4 and α_a, three approximate methods varying in their degree of detail are now presented for the representation of the aerosol absorption.

For (globally) average conditions Ivlev[23] and Toon and Pollock[24] have summarized global aerosol concentrations, particle distributions, and absorption coefficients (or optical depths at 0.55μ $\tau_{0.55}$). For the boundary layer region ($0 < z < 5$km) the Ivlev and Toon-Pollock data are summarized in Table I. The absorption data of Toon and Pollock is systematically below that of Ivlev at the lower altitudes. Perhaps this is in part because it is not averaged over frequency but centered at 0.55μ.

The first and simplest average treatment of aerosols is based on the assumption that local absorption is equal to the global average. The transmission function T_a is then represented as

$$T_a = \exp[-\alpha_a^* z] \qquad (16)$$

with α_a^* taken from Table I.

TABLE I. SUMMARY OF PARTICLE CONCENTRATION AND
ABSORPTION DATA OF IVLEV[23] AND TOON AND POLLOCK[24]

z(km)	Particle Concentration (Ivlev) (cm^{-3})		$\alpha_a^*(km^{-1})$ (From Toon and Pollock calc. from $\tau_{0.55}$)	$\alpha_a^*(km^{-1})$ (Ivlev)
	$r < 0.1$	$2r > 0.1$		
0-1	2×10^4	1.5×10^2	4.2×10^{-2}	1.2×10^{-1}
1-2	3×10^3	8.0×10^1	2.5×10^{-2}	6×10^{-2}
2-3	1×10^3	2.7×10^1	1.6×10^{-2}	3×10^{-2}
3-4	5×10^2	2.0×10^1	0.8×10^{-2}	1.8×10^{-2}
4-5	3×10^2	1.5×10^1	6×10^{-3}	7×10^{-3}

A second approach which allows some detail in the variation of aerosol concentration is the following. The transmission function is represented in terms of the particle density $N(z)$ rather than the mass density ρ_4 as

$$T_a(n_a) = \exp\left[-\hat{\alpha}_a n_a\right] \qquad (17)$$

where

$$n_a = \int_{z_1}^{z_2} N(z)\,dz \qquad (18)$$

From the data of Table I, the absorption coefficient $\hat{\alpha}_a$ may be computed and is tabulated in Table II.

TABLE II. SPECIFIC PARTICLE ABSORPTION
COEFFICIENT $\hat{\alpha}_a$ COMPUTED FROM THE DATA OF TABLE I

z(km)	$\hat{\alpha}_a(\text{cm}^2)$
0-1	6×10^{-3}
1-2	5.2×10^{-3}
2-3	3.75×10^{-3}
3-4	2.94×10^{-3}
4-5	1.41×10^{-3}

The representation in terms of $\hat{\alpha}_a$ would be useful in situations where the particle size distribution could be assumed invariant with respect to total particle density N. One would expect this to be the case for low aerosol densities where aerosol particle-particle interactions are rare. Aerosol absorption would then be a function only of aerosol concentration $N(z)$ with the absorption coefficient $\hat{\alpha}_a$ taken to possess a universal height distribution typical of the global average of Table II. The

number density $N(z)$ is then predicted with a turbulent species transport equation as is done for water vapor or pollutants in existing A.R.A.P. models. Note also that the absorption co- . efficient $\hat{\alpha}_a$ could be, within the limits of the approximations involved, taken as a constant $\hat{\alpha}_a \cong 5 \ 10^{-3} cm^2$ in the 0-3 km region which is the boundary layer region of principal interest.

A third approach similar to the second in level of detail represents the transmission function as

$$\tau(z_1,z_2) = T_v(m_1) \cdot T_g(m_2') \cdot T_\ell(m_3)$$

where m_1 , m_3 are as defined in Eq. (7), but m_2' is constructed to be a composite of clear air molecular absorption and aerosol absorption in the following manner:

$$m_2' = \int_{z_1}^{z_2} (1 + \eta(z)t_r)\rho_g dz \qquad (19)$$

In Eq. (19), ρ_g is the air density, $\eta(z)$ is the mass fraction of aerosol relative to the mass fraction at some reference elevation (typically the surface). The parameter t_r is the reference turbidity defined as the ratio of the absorption co- efficient of the aerosol to the absorption coefficient of clear air at the reference level. Thus, in this approach the aerosol transmission is represented in terms of two parameters: a non- dimensional turbidity profile $\eta(z)$ and a reference turbidity level t_r . Reasonable assumptions may be made for these para- meters for specific calculational cases. For example, in the marine boundary layer, the turbidity primarily arises from sea salt particles turbulently diffused and convected from the surface as is the water vapor. In this case, one may make the turbidity profile $\eta(z)$ similar to the humidity profile.

For values of reference turbidity, Sivkov[25] proposes the following semi-quantitative classification:

t_r	Atmospheric Condition
0	free of aerosols
1	mildly turbid atmosphere
4	highly turbid atmosphere

VI.   REPRESENTATION OF THE UPPER ATMOSPHERE

The mass integrals m_i defined by Eq. (7) extend throughout the entire atmosphere. For the domain of the mass integral which extends above the boundary layer height $z = H_b$ some assumption about the upper atmosphere properties are required. These upper atmosphere characteristics are represented by three model parameters:

t_u = average turbidity of the upper atmosphere

h_u = average humidity of the upper atmosphere

ℓ_u = average liquid water fraction of the upper atmosphere
(If the upper atmosphere is cloudless, $\ell_u = 0$, except for ice clouds)

Let H_o be the atmosphere scale height (H_o = 7994m). Then for the mass integrals that extend into the upper atmosphere, we have

$$m_i = \int_z^H \rho_i dz = \int_z^{H_b} \rho_i dz + (m_u)_i$$

where $(m_u)_i$ is defined as

$$(m_u)_i = \rho_i(z_o)\Delta H$$

and

$$\Delta H \equiv H_o - H_b$$

In particular, for the four mass integrals we have

$$(m_u)_1 = \rho_1(z_o)h_u\Delta H$$

$$(m_u)_2 = \rho_2(z_o)\Delta H$$

$$(m_u)_3 = \rho_1(z_o)\ell_u\Delta H$$

$$(m_u)_2' = \rho_g(z_o)(1 + t_u)\Delta H$$

A-16

VII.   MODEL COMPARISON WITH ATMOSPHERIC MEASUREMENTS

For the purpose of initially verifying the general correct-
ness of the present radiation model, we have selected a comparison
of long wavelength radiation data reported from the International
Radiometersonde Intercomparison Program by Gille and Kuhn[26] and
a verification of short wavelength solar heating predictions of
the model compared to the observations of Reynolds, Vonder Haar,
and Cox[27] in the BOMEX marine boundary layer.

In the case of the Gille-Kuhn intercomparison data, at-
mospheric temperature, pressure, and humidity as measured are used
as inputs to the model from which the long wavelength radiant
fields and cooling rates are predicted. These are then compared
with the measured radiant fields. The results of this comparison
for two typical cases are shown in Figs. 1-6, one for clear skies
and one with high overcast in the upper atmosphere. It can be
seen that the comparison between predicted and experimental values
is reasonable.

As a check on the direct solar heating predictions of the model,
we have computed the direct solar heating rate in the lower marine
boundary layer for conditions generally similar (but not identical
in detail) to that in the BOMEX experiment reported by Reynolds,
Vonder Haar, and Cox[27]. The boundary layer was assumed to have a
reference turbidity of $t_r = 1$ (mildly turbid) and the heating·
rates were averaged over daylight hours to be consistent with the
normalization utilized by Reynolds, et al. The model predicted
heating rate is compared with the measurements in Fig. 7. A
favorable comparison of order of magnitude again results.

VIII. AN APPROXIMATE FORM OF THE TRANSFER EQUATIONS

The transfer Eqs. (1) contain a convolution of the source function gradient over the transmission function of the form

$$\int_{z_1}^{z_2} \tau(z', z_2) \frac{\partial s}{\partial z'} dz'$$

For practical calculations the computation of this convolution integral can be extremely lengthy. An approximate but rapid computation would therefore be desirable. The transmission function $\tau(z', z)$ is a monotone decreasing function of the difference of arguments $z - z'$ vanishes for $z - z' \to \infty$, and is identically unity for $z' = z$. It is easy to show that there exists a suitably defined average $< >$ such that

$$\int_{z_1}^{z_2} \tau(z', z_2) \frac{\partial s}{\partial z'} dz' = <\tau(z', z_2)>_{z_1, z_2} [S(z_2) - S(z_1)] \qquad (20)$$

As an approximation to this average, we shall adopt a simple definition of the average transmission $<\tau>_{z_1, z_2}$ as the transmission function calculated in terms of the arithmetic average of the argument difference, viz:

$$<\tau(z', z)>_{z_1, z_2} = \tau(m_1/2,\ m_2/2,\ m_3/2) \qquad (21)$$

where the m_i are defined as in Eq. (7). The approximation, Eq. (21), of the convolution is computationally extremely rapid. A comparison of the approximate form, Eq. (20), with the exact convolution form, Eqs. (1), is shown in Figs. 8-10.

A-18

IX. CONCLUSION

We conclude that the radiation model we have developed for incorporation in A.R.A.P. atmospheric fluid dynamic calculations yields results which are consistent with the limited experimental radiation measurements available. Further confirmation of its validity will, of course, come in the use of the full fluid-radiative atmospheric equations in predicting marine boundary layer phenomena of general interest.

REFERENCES

1. Goody, R.M., 1964: _Atmospheric Radiation_. Vol. I, Oxford, Clarendon Press, Chapter 9.

2. Goody, R.M., 1964: _Atmospheric Radiation_. Vol. I, Oxford, Clarendon Press, Chapter 2.

3. Ellingson, R.G.: 1962: _A New Longwave Radiative Transfer Model: Calibration and Application to the Tropical Atmosphere_. Dept. of Meteorology, Florida State Univ., Report 72-4.

4. Atwater, M.S., 1966: "Comparison of Numerical Methods for Computing Radiative Temperature Changes in the Atmospheric Boundary Layer," _J. Appl. Meteor._ 5, 824-831.

5. Rodgers, C.D. and C.D. Walshaw, 1966: "The Computation of Infrared Cooling Rate in Planetary Atmospheres," _Quart. J. R. Meteor._ 92, 67-92.

6. Marchuk, G.I., 1967: _Numerical Methods in Weather Prediction_, Gidrometeoizdat, Leningrad, Chapter 7.

7. Ellingson, R.G, in J.C. Gille and P.M. Kuhn, 1972: _The International Radiometersonde Intercomparison Programme (1970-71)_. W.M.O. No. 358, Geneva.

8. Feigel'son, E.M., 1970: _Radiant Heat Transfer in a Cloudy Atmosphere_. Gidrometeorologicheskoe Izadatel'stro Leningrad (English trans. Jerusalem, 1973), Chapter III.

9. Elsasser, W.H., 1942: "Heat Transfer by Infrared Radiation in the Atmosphere," _Harvard Meteorological Studies_, No. 6.

10. Feigel'son, E.M., 1970: _Radiant Heat Transfer in a Cloudy Atmosphere_. Gidrometeorologicheskoe Izadatel'stro Leningrad (English trans. Jerusalem, 1973), p. 83.

11. Davis, P.A. and W. Viezee, 1964:"A Model for Computing Infrared Transmission through Atmospheric Water Vapor and Carbon Dioxide." _J. Geophys. Rev._ 69, 3785-3794.

12. Feigel'son, E.M., 1970: _Radiant Heat Transfer in a Cloudy Atmosphere_, Gidrometeorologicheskeo Izadatel'stro Leningrad (English trans. Jerusalem, 1973), p. 88.

13. Gradus, L.M., Kh. Yu. Niilisk, and E.M. Feigel'son, 1968: "Integral Transmission Function for Cloudy Conditions," _Izvestizr ANSSSR, Fizika Atmosfery i Okeana_, No. 4.

14. Herman, B., 1962: "Infrared Absorption, Scattering, and Total Attenuation Cross Sections for Water Vapor," Q.J. Roy. Meteor. Soc. 88, No. 376.

15. Zel'manovich, I.L. and K.S. Shifrin, 1968: Tables on Scattering of Light. Vol.3, Leningrad, Gidrometeoizdat.

16. Sivkov, S.I., 1968: Computation of Solar Radiation Characteristics. Gidrometeorslogicheskoe Izdatel'stro, Leningrad (English Translation Jerusalem, 1971), p. 72.

17. Sivkov, S.I., 1968: Computation of Solar Radiation Characteristics. Gidrometeorologicheskoe Izdatel'stro, Leningrad (English Translation Jerusalem, 1971), Table 16, p. 75.

18. Manabe, S. and R.F. Strickler, 1964: "Thermal Equilibrium of the Atmosphere with a Convective Adjustment," J. Atmos. Sci. 21, (Fig. A-4), pp. 361-385.

19. Eltermann, L., R. Wexler, and D.T. Chang, 1969: "Features of Tropospheric and Stratospheric Dust," Appl. Opt. 8, No. 5, pp. 893-904.

20. Feigel'son, E.M., 1964: Light and Heat Radiation in Stratus Clouds. Izdatel'stro "Nauka" Moscow (English Translation Jerusalem, 1966), p. 48.

21. Feigel'son, E.M., 1964: Light and Heat Radiation in Stratus Clouds. Izdatel'stro "Nauka" Moscow (English Translation Jerusalem, 1966), Table I.4.21, p. 50.

22. Kondratyev, K. Ya., 1972: Radiation Processes in the Atmosphere. W.M.O. No. 309, Geneva, p. 100.

23. Ivlev, L.S., 1969: "An Aerosol Model of the Atmosphere," Probl. of Atm. Phys., Leningrad Univ. Publ. , pp. 125-160. (Also Kondratyev, K. Ya. (1972) Ibid., p. 101).

24. Toon, O.B. and J.B. Pollock, 1976: "A Global Average Model of Atmospheric Aerosols for Radiative Transfer Calculations," J. Appl. Meteor. 15, pp. 225-246.

25. Sivkov, S.I., 1968: Computation of Solar Radiation Characteristics. Gidrometeorologicheskoe Izdatel'stro, Leningrad (English Translation Jerusalem, 1971), p. 75.

26. Gille, .C., and P.M. Kuhn, 1972: The International Radiometersonde Intercomparison Programme (1970-71). W.M.O. No. 358, Geneva.

27. Reynolds, D.W., Vonder Haar, T.H., and S.K. Cox, 1975: "The Effect of Solar Radiation Absorption in the Tropical Troposphere," J. Appl. Meteor. 14, 4, P. 433.
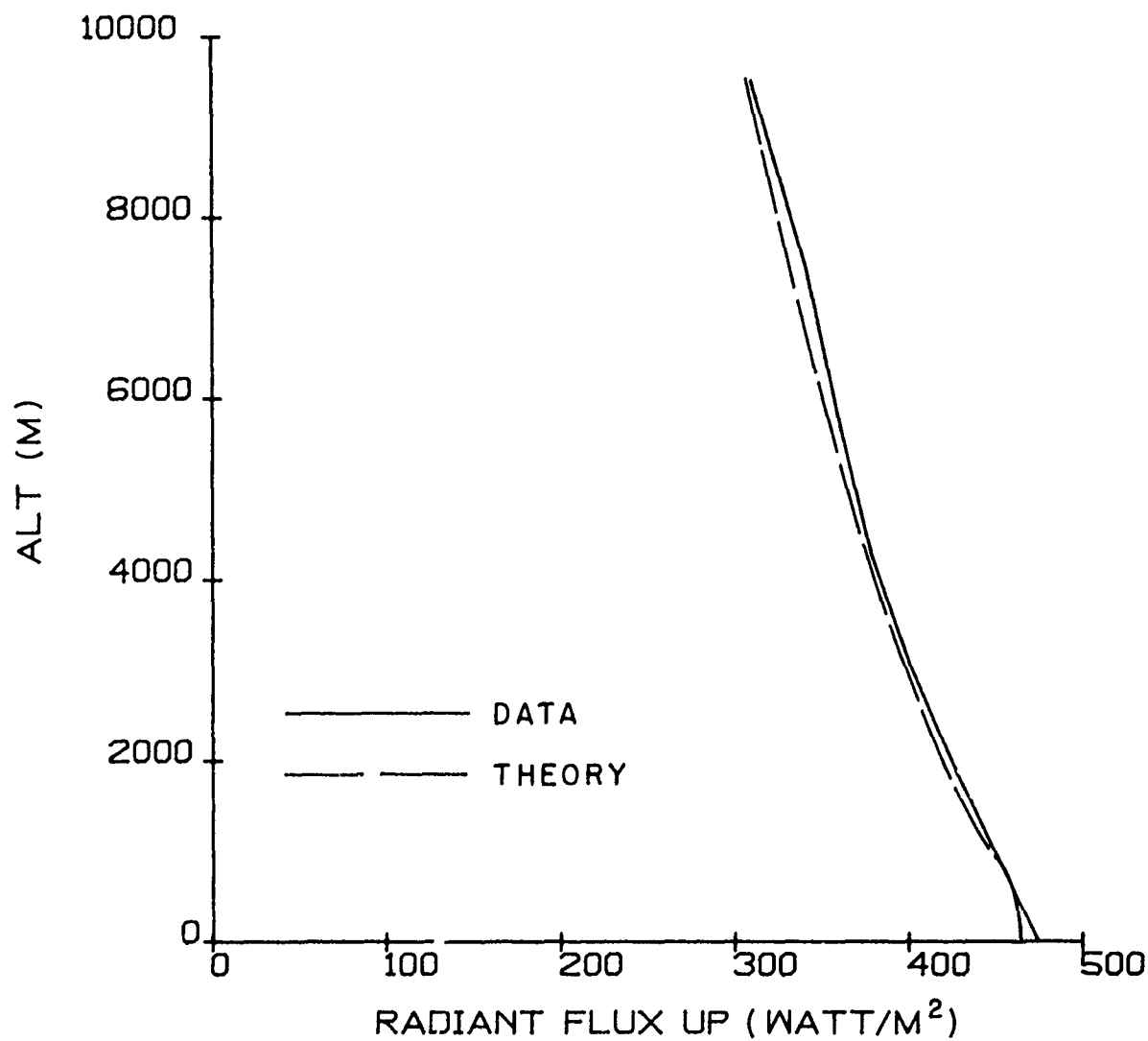
Figure A-1.   Upward long wavelength radiant flux in the earth's
              atmosphere corresponding to Case D-3, clear skies,
              J.C. Gille and P.M. Kuhn[26] compared to radiation
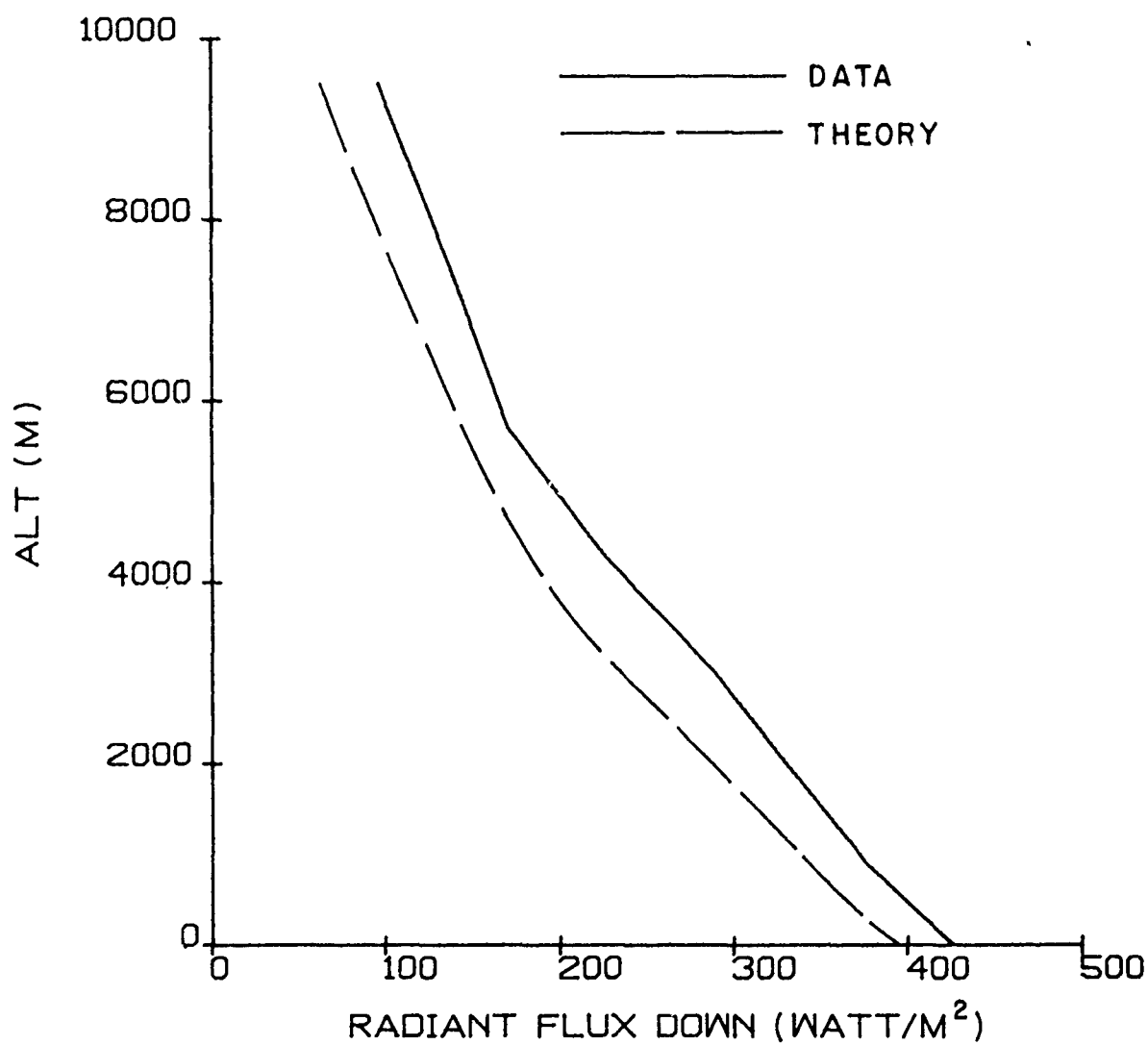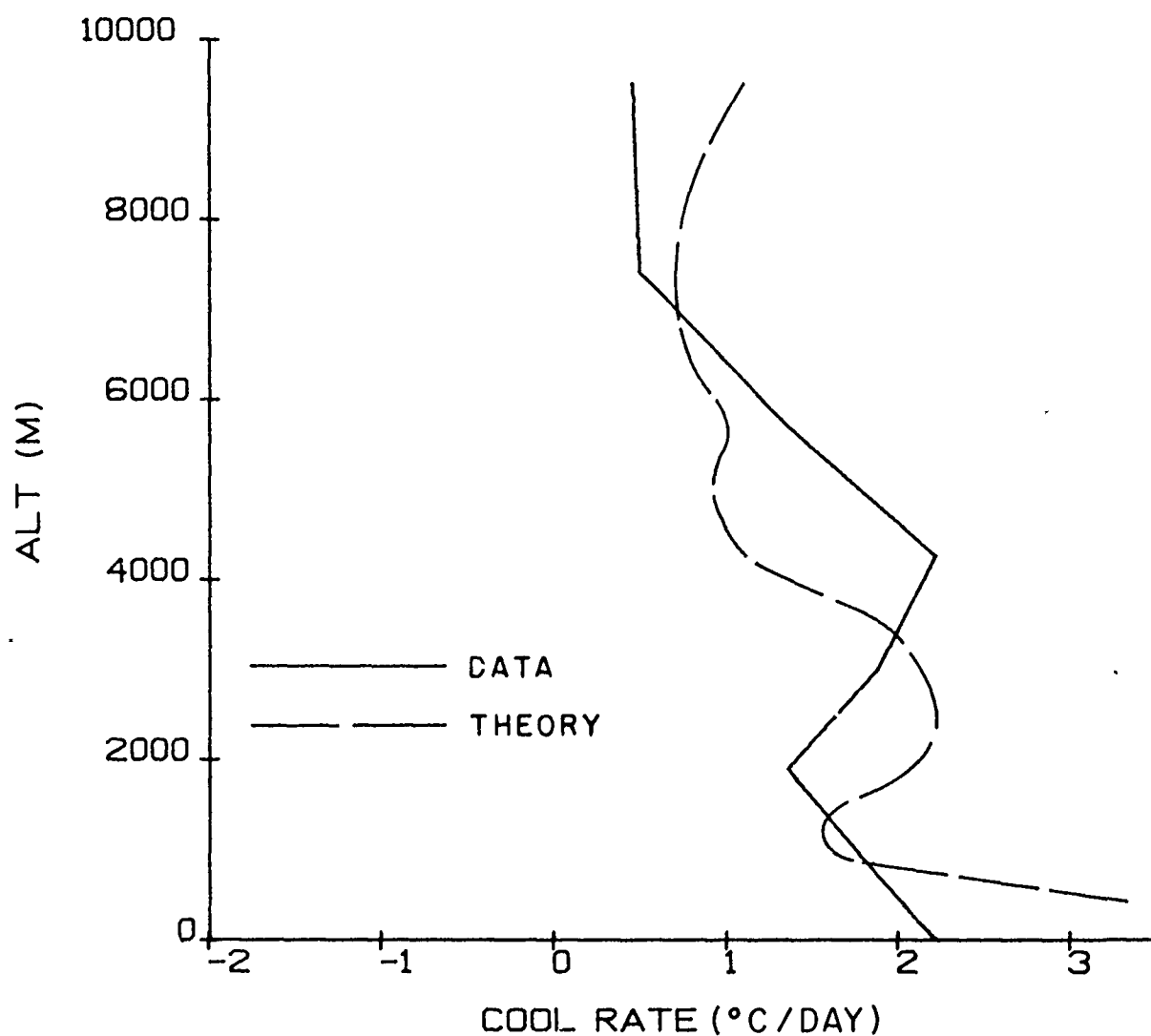   model predictions.

Figure A-2.   Downward long wavelength radiant flux in the earth's
              atmosphere corresponding to Case D-3, clear skies,
              J.C. Gille and P.M. Kuhn[26] compared to radiation
              model predictions.

Figure A-3.   Comparison of radiation model predictions and experimental
             summary of J.C. Gille and P.M. Kuhn[16] of atmospheric long
             wavelength cooling rate, Case D-3, clear skies.
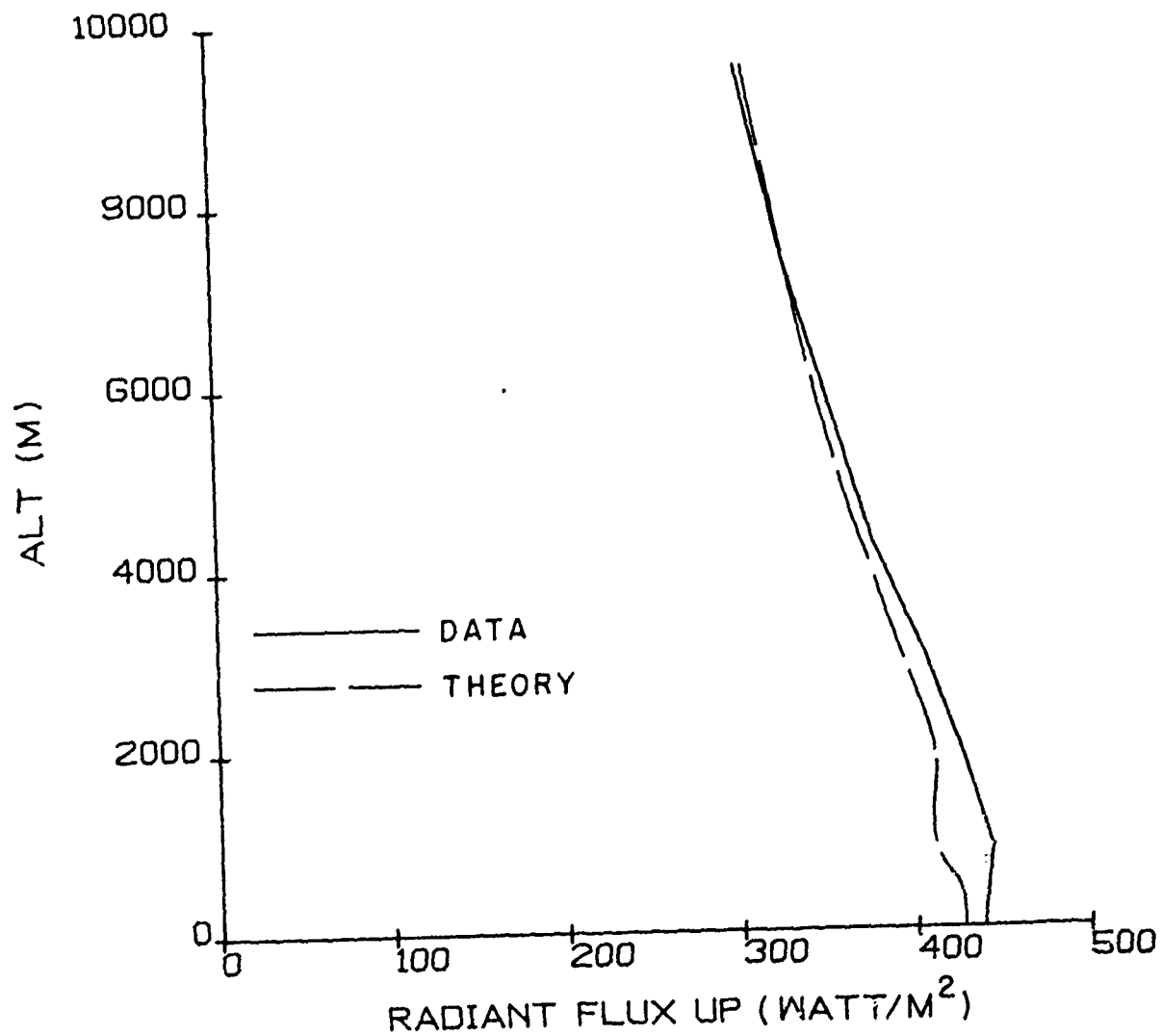
Figure A-4. Upward long wavelength radiant flux, Case D-5 (overcast) of J.C. Gille and P.M. Kuhn[26] compared to radiation model predictions.
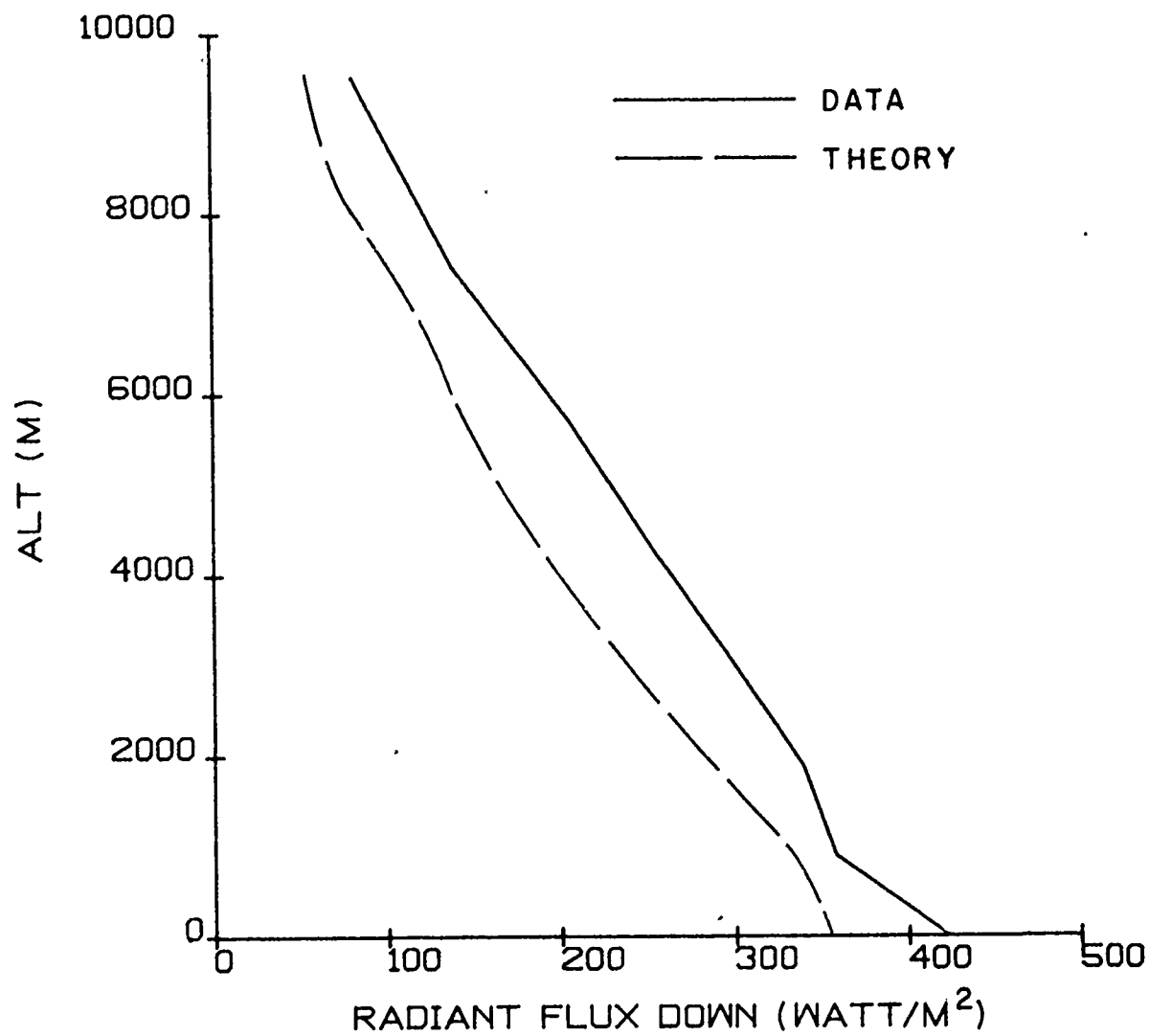
Figure A-5. Downward long wavelength radiant flux, Case D-5 (overcast) of J.C. Gille and P.M. Kuhn[26] compared to radiation model predictions.
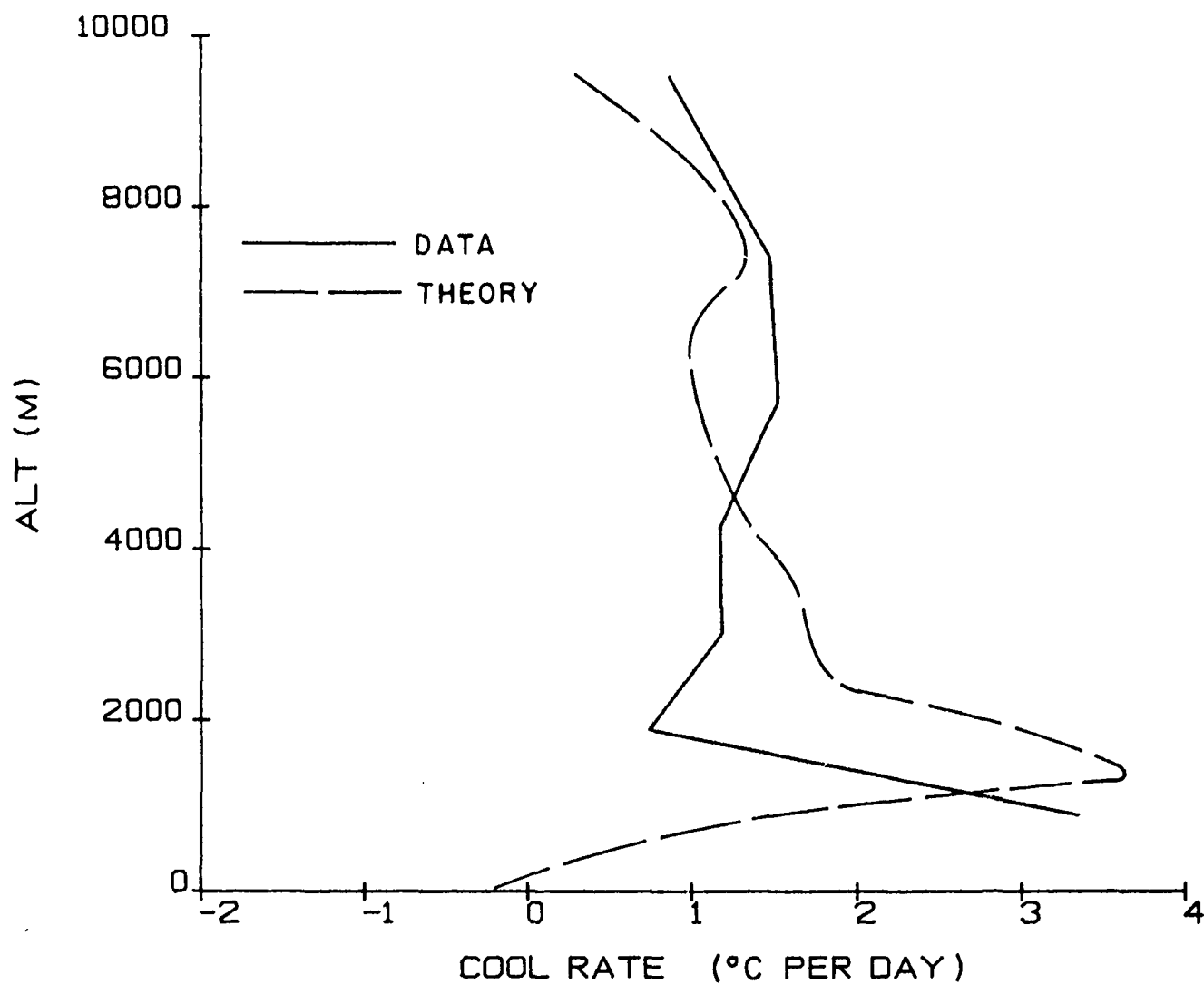
Figure A-6. Comparison of radiation model predictions and experimental
summary of J.C. Gille and P.M. Kuhn[26] of atmospheric long
wavelength cooling rate, Case D-5 (overcast).
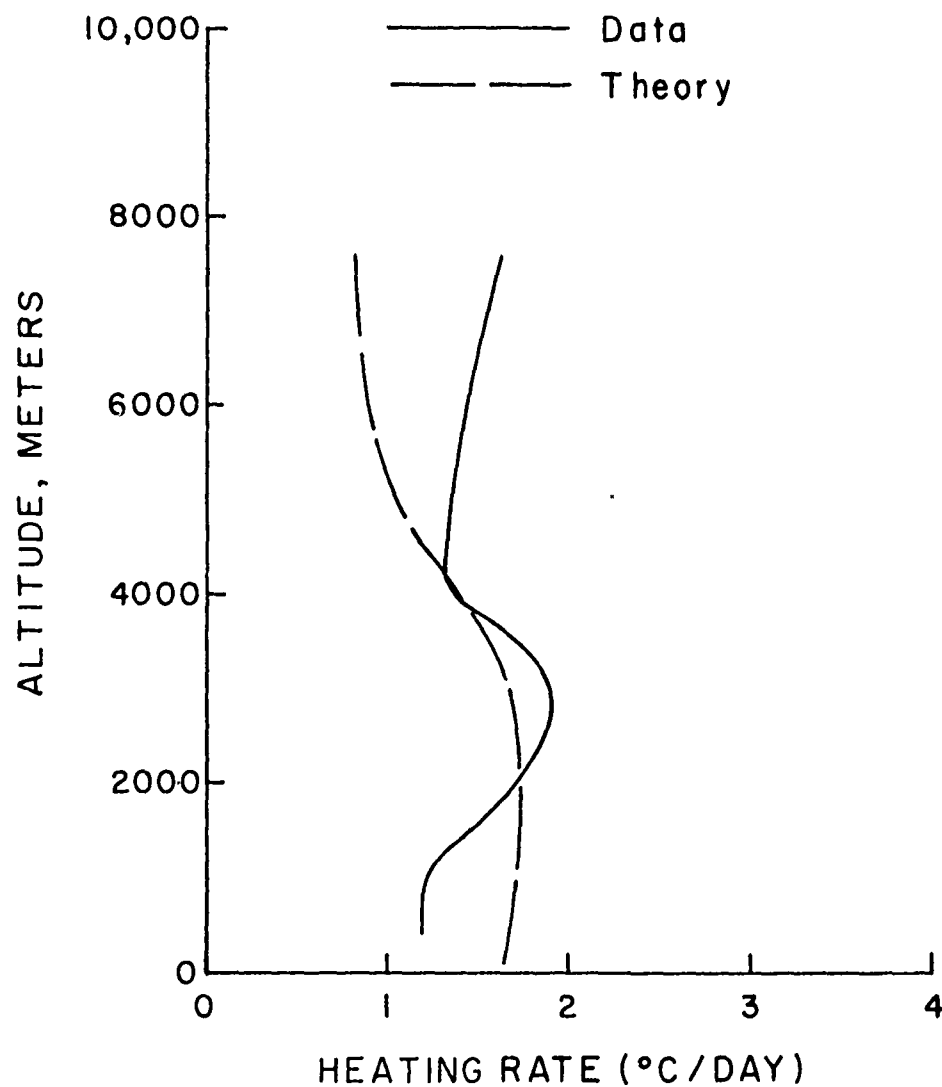
Figure A-7. Comparison of direct solar heating rate predicted by the radiation model and measured heating rates of Reynolds, et al.[27]. Bulge in the experimental data is due to wind-borne Sahara dust between 2000-4000 m.
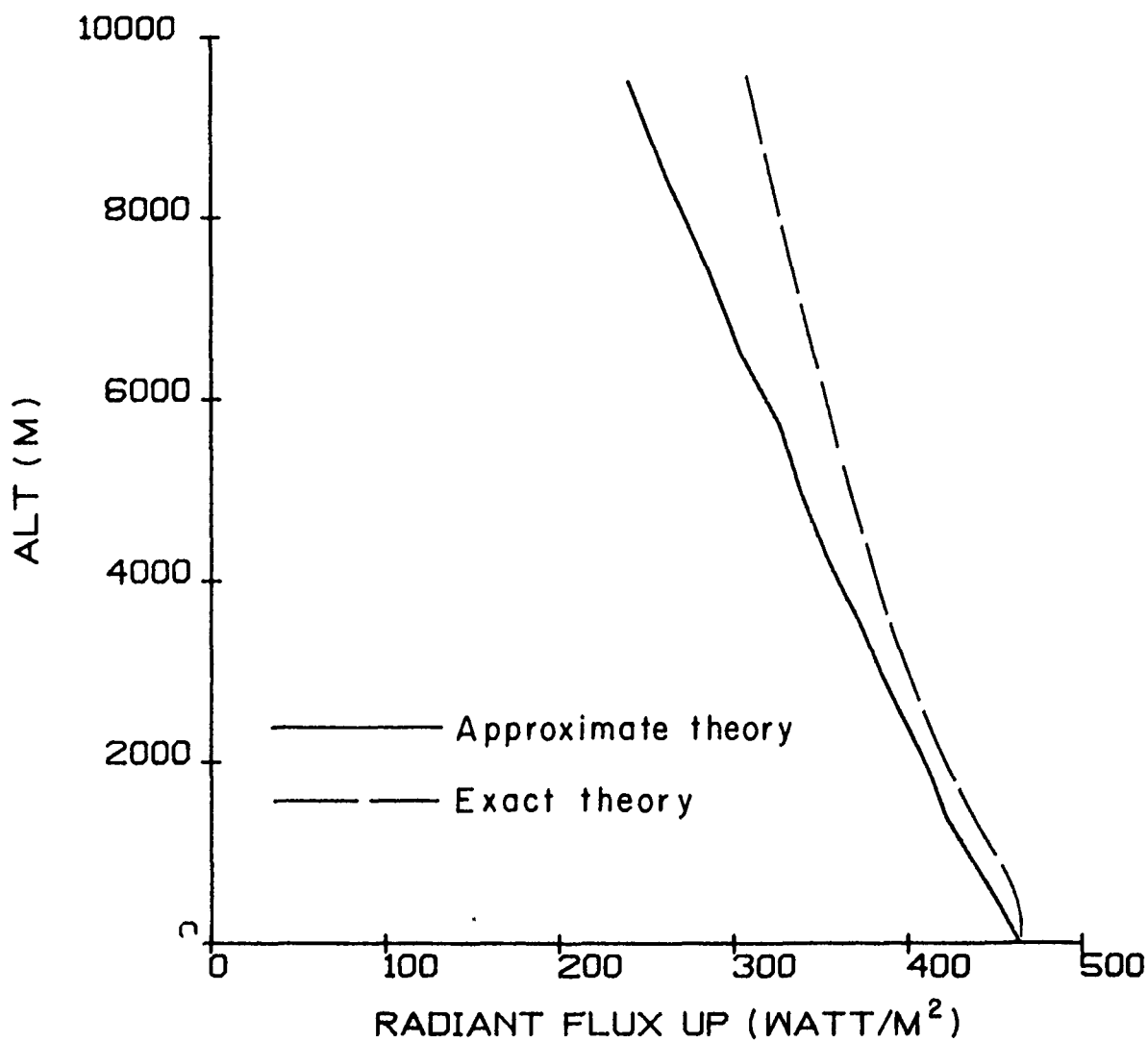
Figure A-8. Comparison of results for approximate and exact convolution
integrals [Eqs. (1), Eqs. (20)] for the D-3 Case of
Gille and Kuhn for upward radiant flux.
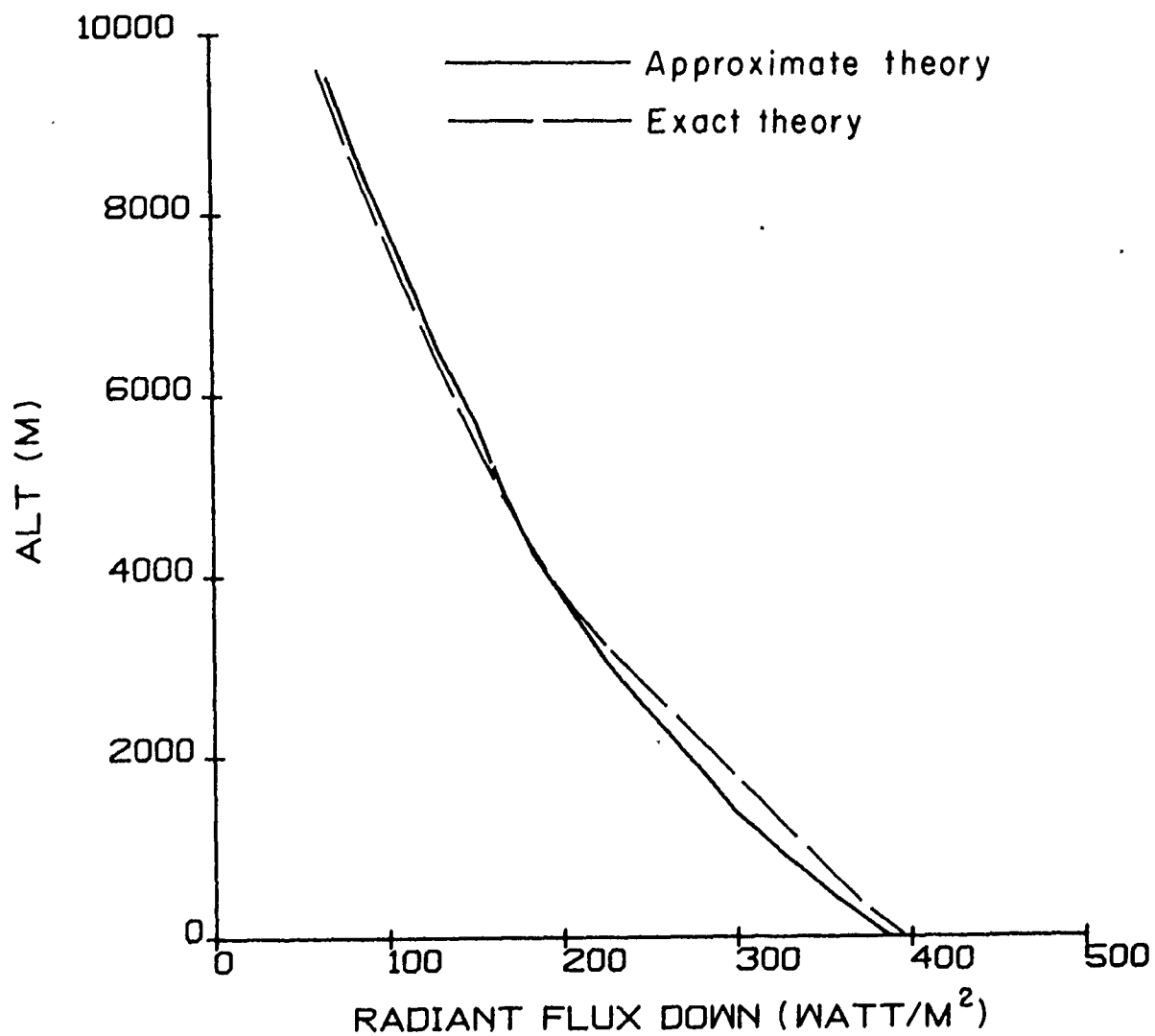
Figure A-9. Comparison of approximate and exact downward radiant flux for conditions of Fig. 8.
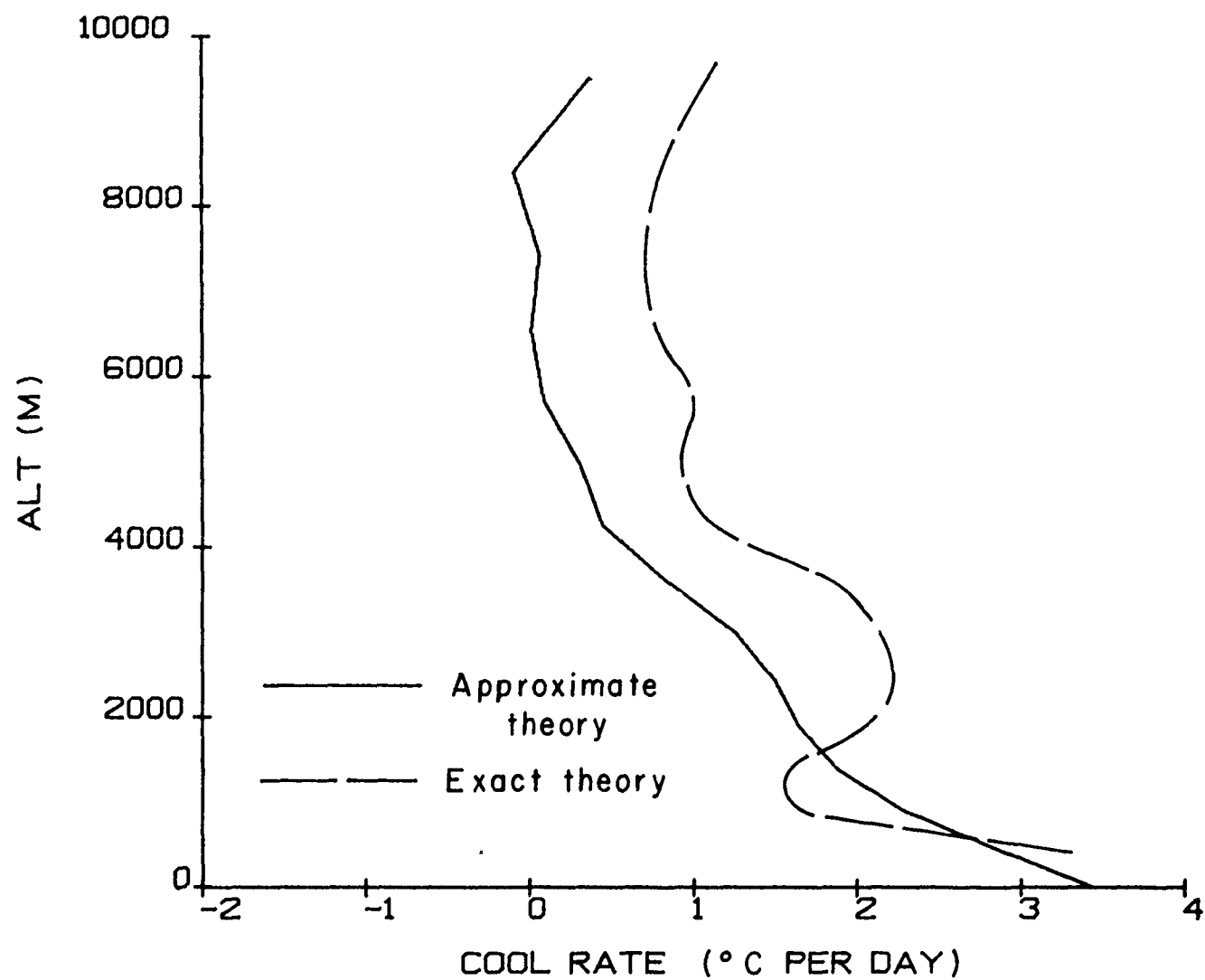
Figure A-10. Comparison of approximate and exact cooling rates for conditions of Fig. 8.

APPENDIX B

A SECOND-ORDER CLOSURE MODEL
OF TURBULENT TRANSPORT IN THE
COASTAL PLANETARY BOUNDARY LAYER

W. S. Lewellen

M. E. Teske

A SECOND-ORDER CLOSURE MODEL OF TURBULENT TRANSPORT
IN THE COASTAL PLANETARY BOUNDARY LAYER[*]

W. S. Lewellen and M. E. Teske
Aeronautical Research Associates of Princeton, Inc.
Princeton, New Jersey

INTRODUCTION

The diurnal variation in the planetary boundary layer is quite different over land than it is over a large body of water. This variation leads to the familiar sea-breeze circulation pattern near the shore. Many of the characteristics of lake/sea breezes have been described in a review by Lyons (1975) with particular emphasis on pollutant transport in such an environment. The most recent attempts to model this phenomenon have been the work of Pielke and Mahrer (1975) and Mak and Walsh (1976). In order to simulate the stability variation of the turbulent transport processes, an essential part of the sea-breeze phenomenon, both works use an empirically assumed eddy viscosity that is a function of both space and time.

Turbulent models based on second-order closur⁻ᵉ proving to be very useful for solvi ₋ turbulent transport of momentum, energy, and species in the planetary boundary layer (Lewellen and Teske, 1975; Wyngaard, et al., 1974; Mellor and Yamada, 1974). The purpose of this paper is to present some preliminary results of a calculation of the sea-breeze circulation using a second-order closure model of turbulence. Such an approach eliminates the need to specify an empirical eddy viscosity variation.

REVIEW OF SECOND-ORDER CLOSURE MODEL

Work at A.R.A.P. over the last few years has led to the development of an invariant, second-order closure technique for the determination of the Reynolds stress terms $\overline{u_i u_j}$, and the turbulent flux of potential temperature $\overline{u_i \theta}$ and flux of humidity mixing ratio $\overline{u_i H}$, that appear in the mean momentum, energy, and humidity equations. By manipulating the fluctuating equations of motion, one can derive a set of exact equations for the needed second-order correlations and the further correlations $\overline{\theta^2}$, $\overline{\theta H}$ and $\overline{H^2}$ that appear (Donaldson, 1973). The task of second-order closure is to model the resulting terms involving third-order correlations and other unknown second-order correlations as functions of the known second-order correlations, mean flow gradients, and proper scaling and modeling constants, and thus close the equation set. To do this we choose the simplest models that have proper tensor symmetry, dimensionalization, and desired physical properties; make a consistent selection of the values of the modeling constants; then leave these values fixed when computing new flow geometries. Lewellen and Teske (1975) contains an extensive discussion of the modeling procedure and an examination of the many flow geometries used to evaluate and verify the selection of modeling constants. Modeling predictions for more complicated flows include the diurnal planetary boundary layer (Lewellen, et al., 1974), stratified flows (Lewellen, et al., 1976), and vortex wakes (Bilanin, et al., 1976).

A solution of the full set of equations (21 including a differential equation for the turbulent scale length) is a formidable numerical problem. For the present calculation, we elect to make a simplifying assumption to the turbulent correlation equations by treating them in a quasi-steady, nondiffusive limit. The partial differential equations for the second-order correlations in this boundary layer problem then reduce to algebraic expressions as a function of the vertical gradients of the two mean horizontal wind components, the vertical potential temperature, and the humidity mixing ratio. The full dynamic behavior is also retained for the turbulent kinetic energy q^2 and the turbulent scale Λ. The resulting algebraic equations for the 14 turbulent correlations may be solved explicitly (Lewellen, et al., 1974).

The calculations are performed using a computer code that solves the two-dimensional, unsteady equations of motion for the mean velocities U and V, virtual temperature θ_v, humidity H, turbulent kinetic energy q^2 and turbulent

scale length Λ. Turbulent correlations $\overline{u_i u_j}$, $\overline{u_i \theta_v}$, $\overline{\theta_v^2}$, $\overline{u_i \Pi}$, $\overline{\theta_v \Pi}$ and $\overline{\Pi^2}$ are found by applying the quasi-equilibrium approximation discussed earlier. Details of the finite differencing technique employed and the implicit solution technique used may be found in Lewellen and Teske (1975).

Since the vertical velocity is of higher order in the planetary boundary layer, the vertical momentum equation reduces to the hydrostatic approximation. The vertical velocity is then determined from continuity via a stream function-vorticity approach, with the vorticity determined directly from the horizontal momentum equation. The Poisson equation for ψ is solved directly by an application of the BLKTRI general elliptic solver developed by Swarztrauber and Sweet (1975).

The advection terms in the present calculation are upwind differenced. This undoubtedly adds horizontal diffusion to the calculation. However, the principal balance in the present calculation is between vertical diffusion and horizontal advection which should dominate the horizontal numerical diffusion. The character of the present result should be essentially correct. The largest errors introduced are probably due to the relatively large Δy grid spacing which varies from 3 to 18 km.

FORMULATION OF THE SAMPLE CALCULATION

In the present calculation the land and water surface temperature is taken equal to 290°K at $t = 0$. The land surface temperature is then permitted to add a perturbation which varies with time as

$$\theta_{LS} = 10 \sin \frac{2\pi t}{86400 \text{ sec}} \; ^{\circ}C \qquad (1)$$

while the water surface temperature is held fixed. Equation (1) ignores any spatial variation of the land surface temperature. To account for this variation correctly, it would be necessary to solve for heat flow in the top layer of the land soil in a completely coupled manner with the boundary layer calculation.

The surface temperature of shallow coastal water may also have a slight diurnal variation. However, we believe this ideal problem of a land mass undergoing a sine wave variation in its surface temperature, bounded by a constant temperature water reservoir, exhibits the essential features of the diurnal variation in the sea-breeze circulation. We have included a surface roughness difference between the land and the water with $z_0 = 0.1$m for the land and 2.3×10^{-5} m for the water.

In partial simulation of infrared radiation cooling from the moist marine air, we have also included a thermal radiation source term in the energy equation equal to

$$\dot{Q}_r = -2 \times 10^{-4} (^{\circ}C/\text{sec}) \exp(-z/500 \text{ m}) \quad (2)$$

In a real boundary layer this radiation flux divergence term is strongly coupled to the flow variables, particularly the water vapor distribution. In this preliminary model, the simple cooling function in Eq. (2) is incorporated to permit the boundary layer over the water surface to maintain a slight instability as observed over the ocean.

The computation is performed over a domain stretching from 126 km on either side of the shoreline, with a vertical ceiling at 1700 m. One of the principal difficulties of the computation is the appropriate treatment of the internal gravity waves at the open boundaries. In this calculation horizontal diffusion is increased smoothly as the boundary is approached to damp out any waves and prevent reflection back into the domain of interest. The results shown below are confined to 80 km on either side of the shoreline, since the wave liner influences the results between 80 and 126 km.

The geostrophic wind is aligned with the coastline and has a value of either ±5 m/sec. With the land surface on the right in the figures shown, the plus sign corresponds to flow out of the paper.

The other variables which significantly affect the results are the initial height of the inversion layer and the lapse rate above the boundary layer. Above $z = 1100$ m the vertical potential temperature gradient is set at -0.001°C/m initially.

RESULTS

Figure 1 shows the time history of the two components of horizontal velocity at the shoreline ($y = 0$) as a function of altitude. The component perpendicular to the shoreline, V, is directed toward the land (positive) below approximately 400 m, except for a brief period near the end of the cycle. The return flow at altitude is substantially reduced in magnitude but occurs over a larger region. The sea breeze velocity increases as the land surface temperature increases, with its maximum value occurring about an hour after the maximum surface temperature is reached at 6 hours. The reduction in the sea breeze lags far behind the decrease in the surface temperature so that very little reversal or land breeze occurs (only near 21 hours). The velocity component parallel to the shoreline, U, reaches a maximum value near the point (12 hours) where the land surface temperature goes through its zero point.
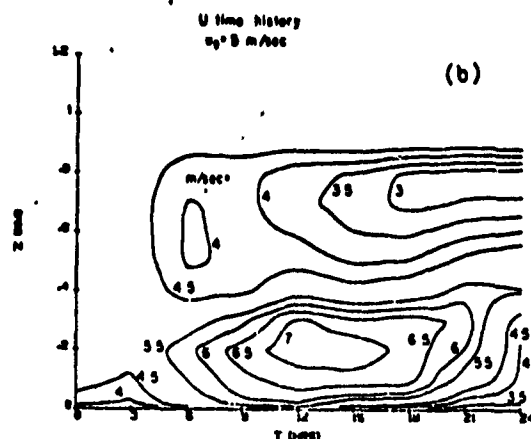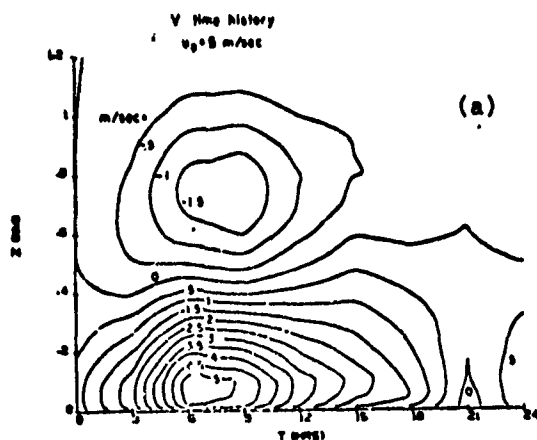
Fig. 1. Time histories of the horizontal wind components at the shoreline (y = 0) for u_g = 5 m/sec: (a) V velocity normal to the shore; (b) U velocity parallel to the shore. A positive value of V is sea breeze.

The pressure gradient induced by the temperature difference in the boundary layer over the land and that over the water appears to first yield a wind velocity down the gradient, and then the wind vector swings around to be perpendicular to the pressure gradient in the same manner as the geostrophic wind balancing the geostrophic pressure gradient. This gradual turning of the direction of the wind in the course of the diurnal cycle is present in observations (Lyons, 1975) and appears in previous models (e.g., Neumann and Mahrer, 1971).

When the geostrophic wind is reversed, with other conditions unchanged, the maximum value of the sea breeze is reduced substantially, and a land breeze occurs for approximately one-fourth of the cycle as seen in Fig. 2. The parallel velocity component completely changes its character and even shows a slight flow reversal near 15 hours. Although the geostrophic wind is aligned with the shore-line in both cases, the Ekman-type spiral of the wind vector in the layer tends to add to the sea breeze in Fig. 1 and subtract (or add to the land breeze) in Fig. 2. The times and altitudes at which the wind parallel to the shoreline is amplified or retarded are interchanged between Figs. 1b and 2b.

The spatial variation of the sea breeze circulation at 9 hours (3 hours after the maximum land surface temperature is reached) is shown in terms of the two-dimensional streamfunction in Fig. 3. A positive value corresponds to volume flow toward the land. A rather sharp sea breeze front occurs for both orientations of the geostrophic wind, but as might be expected the front is sharpest when the geostrophic pressure gradient leads to a slight opposing wind. In this case (u_g = -5 m/sec), a stagnation point occurs at the leading edge of the front. The maximum vertical velocity occurring in this front is about 0.09 m/sec.
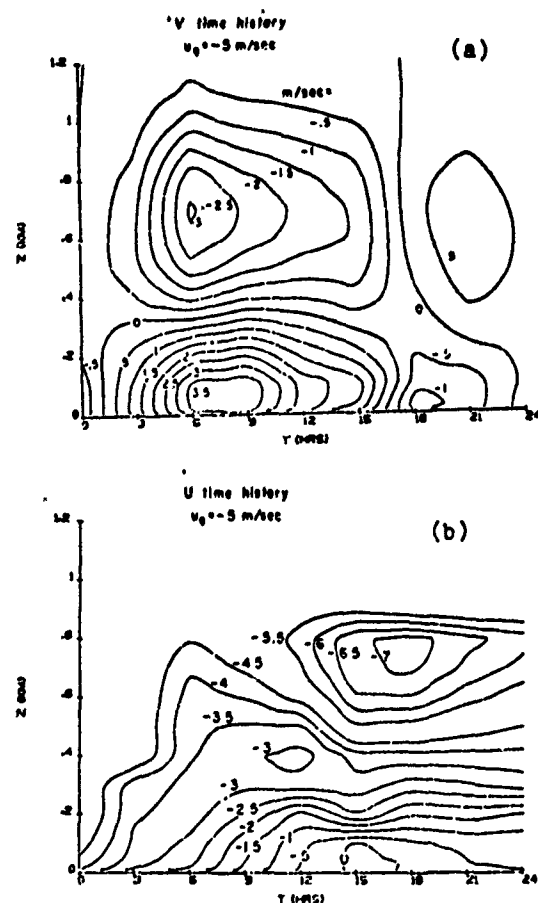
Fig. 2. Time histories at the shoreline (y = 0) for u_g = -5 m/sec: (a) V velocity; (b) U velocity.

The closing of the circulation cell occurs over a wide area. In fact, there is some question as to just how far the return flow would extend out over the water at a later hour since the circulation zone has grown to such a size that we can no longer say with confidence that it is unaffected by the placement of our computational boundaries.
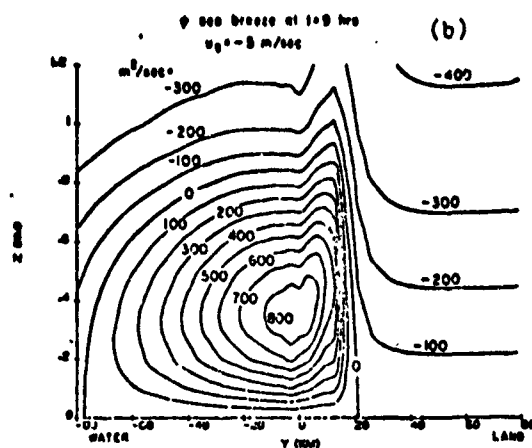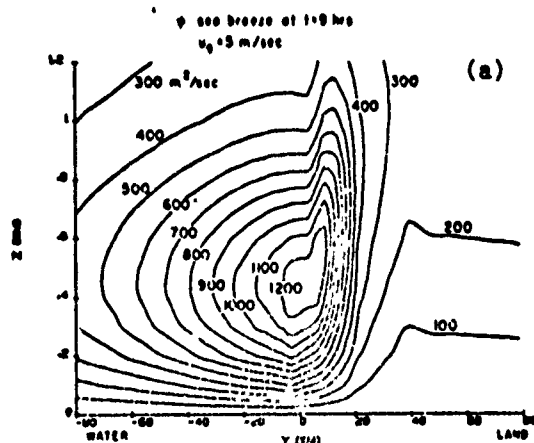
Fig. 3. Contour lines of constant ψ streamfunction for the sea breeze simulation at 9 hrs. after the land temperature begins to increase: (a) $u_g = 5$ m/sec; (b) $u_g = -5$ m/sec. The water is on the left ($y < 0$); the land on the right ($y \gtrless 0$).

The spatial distributions of the horizontal wind occurring at the same time as Fig. 3b are shown in Fig. 4. The sea breeze extends a little more than 20 km inland at this time. The return flow has a velocity V of about one-half of the sea breeze and is spread over a layer about twice as deep. The U component of the wind near the leading edge of the front is reduced in amplitude below its geostrophic value and increased significantly above its geostrophic value over the water in the recirculating zone.

Isolines of turbulent kinetic energy and humidity mixing ratio are shown for this time and geostrophic wind direction in Fig. 5. As expected, the most turbulent region is in the sea breeze front, with the values of q^2 occurring over the water (maximum of about 0.14 m^2/s^2), much lower than those present over the land. The humidity is swept along onto the shore with the sea breeze front, and then stopped abruptly by the relatively dry air over the land. If the computation were allowed to run for several days, the humidity would build up from the water surface source until clouds form at different points of the cycle. Such phenomena must await future calculations.

The sea breeze front at the time of Figs. 3-5 appears to be much more narrow than can be well defined by the grid spacing used in this computation, since it extends over only a few grid points. Based on a separate calculation using a Δy of 200 m over the reduced domain extending from 200 m on the water side of the shoreline to 6 km inland, it appears that the front is more nearly 1-2 km thick rather than the 10-20 km implied by Fig. 3b. This reduction in front thickness also increases the vertical velocity within it by an order of magnitude. A detailed, accurate solution of the front structure would not only require going to a finer mesh, but also relaxing the hydrostatic approximation.
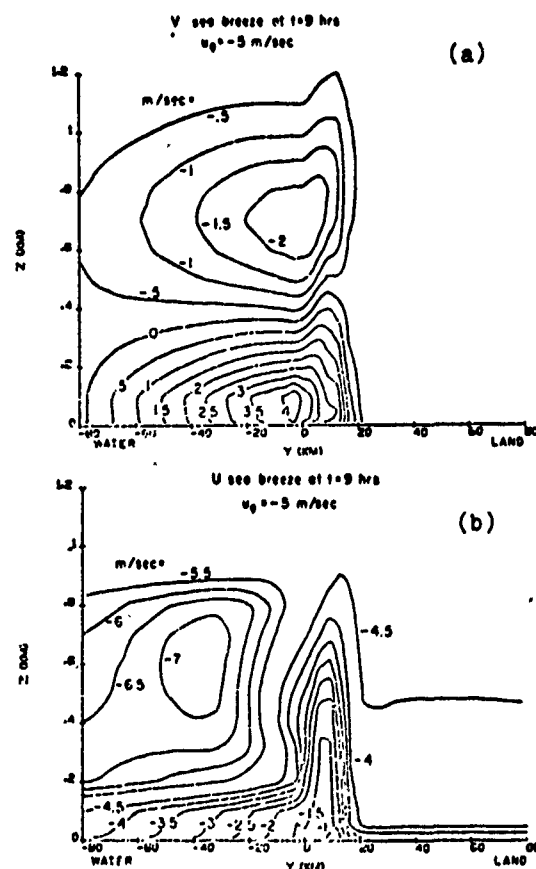

Fig. 4. Contours of constant horizontal velocity at 9 hrs. after initialization for $u_g = -5$ m/sec: (a) V velocity; (b) U velocity.

Figure 6 is a comparison of the vertical potential temperature isolines at 9 hours with those occurring at 18 hours. This figure demonstrates why there is such a large asymmetry between the day time (9 hours) sea breeze and the night time (18 hours) land breeze even when the surface temperature differential is symmetrical. During the day, the warmer land temperature leads to an unstable boundary
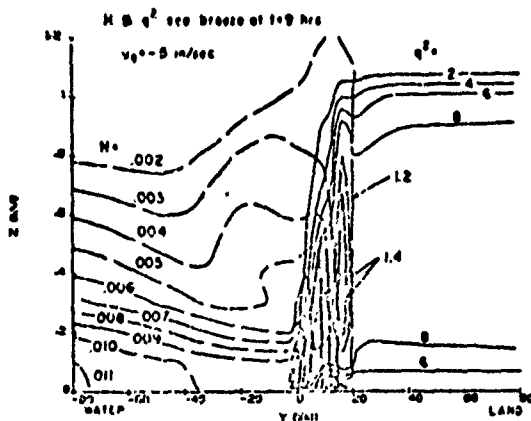
Fig. 5. Composite contours of constant humidity (- -) and turbulent kinetic energy (——) at 9 hrs. after initialization for $u_g = -5$ m/sec.

layer flow which permits the temperature differential to occur over a fairly thick layer. During the night, the surface cooling induces a stable boundary layer flow with the temperature differential restricted to a shallow layer. In previous sea breeze models occurring in the literature, this effect had to be simulated by imposing an empirical eddy diffusivity difference. The effect occurs naturally in the present turbulent model. The cooling over the water, evident in Fig. 6, is a result of the long-wave cooling input with Eq. (2).

The horizontal velocity components present at 18 hours into the cycle are shown in Fig. 7. At this point, the land surface temperature is 280°K. The return flow from the land breeze, i.e., the positive V above the surface, is almost nonexistent with a maximum value of 0.35 m/sec. A large super-geostrophic wind parallel to the coastline exists over the breadth of the land breeze region above 400 m. Velocity reversal occurs at the surface between the shoreline and 60 km inland. It should be noted that the flow is not purely periodic in that conditions at $t = 24$ hrs. do not return to coincide with conditions at $t = 0$.

CONCLUDING REMARKS

A model of turbulence based on second-order closure has been applied to the atmospheric boundary layer in the vicinity of a shoreline. The model is based on solving dynamic, partial differential equations for the turbulent flux of momentum, heat, and moisture. These equations are obtained by second-order closure of the equations for the ensemble-averaged, single-point moments of the fluctuating variables. The numerical model also predicts the unsteady, two-dimensional variations of the mean values, and variances of velocity, potential temperature, and moisture.
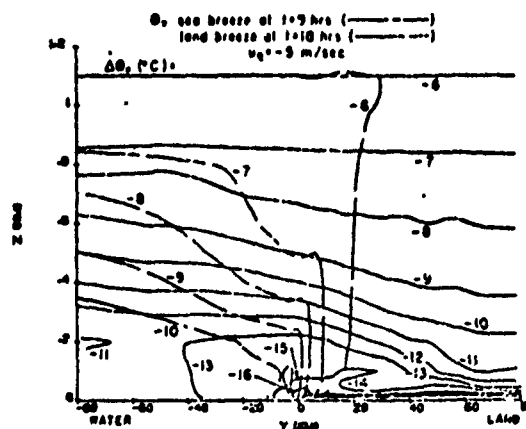

Fig. 6. Composite contours of the departure of the virtual potential temperature from 300°K at 9 hrs. (- -) and 18 hrs. (——) after initialization of the simulation. In the former case, $\theta_{land} = -5°C$, while at the latter, $\theta_{land} = -20°C$.
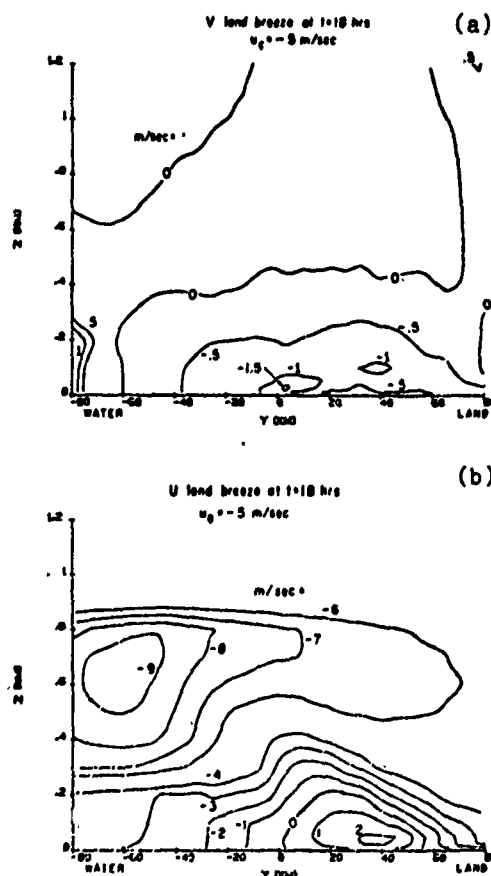

Fig. 7. Contours of constant horizontal velocity at 18 hrs. after initialization for $u_g = -5$ m/sec: (a) V velocity; (b) U velocity.

Calculations have been made for a typical diurnal variation in the surface temperature difference between the land and water with the geostrophic pressure distribution held constant. The resulting

B-5

diurnal variation in the sea breeze induced by the strong stability differences in the boundary layer response over the land and that over the water produced a strong asymmetry between the sea-breeze and the land-breeze circulation patterns. This difference was predicted by the model without the need to introduce any new empirical information into the model. The sensitivity of the sea breeze circulation to the orientation of the geostrophic wind to the shoreline has also been discussed.

REFERENCES

Bilanin, A.J., M.E. Teske, C. duP. Donaldson, and R.S. Snedeker, 1974: Viscous Effects in Aircraft Trailing Vortices. Proceedings NASA Symposium on Wake Vortex Minimization, Wash. D.C., Feb. 25-26, pp. 55-122.

Donaldson, C. duP., 1973: Atmospheric Turbulence and the Dispersal of Atmospheric Pollutants. AMS Workshop on Micrometeorology (D.A. Haugen, ed.), Science Press, Boston, pp. 313-390.

Lewellen, W.S. and M.E. Teske, 1975: Turbulence Modeling and its Application to Atmospheric Diffusion. EPA-600/4-75-016.

Lewellen, W.S., M.E. Teske, and C. duP. Donaldson, 1974: Turbulence Model of Diurnal Variations in the Planetary Boundary Layer. Proceedings 1974 Heat Transfer and Fluid Mechanics Institute (L.R. Davis and R.E. Wilson, eds.), Stanford Univ. Press, Stanford, pp. 301-319.

Lewellen, W.S., M.E. Teske, and C. duP. Donaldson, 1976: Variable Density Flows Computed by a Second-Order Closure Description of Turbulence. AIAA J. 14, pp. 382-387.

Lyons, W.A., 1975: Turbulent Diffusion and Pollutant Transport in Shoreline Environments. Lectures on Air Pollution and Environmental Impact Analyses, AMS, pp. 136-208.

Mak, M.N. and J.E. Walsh, 1976: On the Relative Intensities of Sea and Land Breezes. J.A.S. 33, pp. 242-251.

Mellor, G.L. and T. Yamada, 1974: A Hierarchy of Turbulence Closure Models for Planetary Boundary Layers. J. Atmos. Sci., 31, pp. 1791-1806.

Neumann, J. and Y. Mahrer, 1971: A Theoretical Study of the Land and Sea Breeze Circulation. J.A.S. 28, pp. 532-542.

Pielke, R.A. and Y. Mahrer, 1975: Representation of the Heated Planetary Boundary Layer in Mesoscale Models with Coarse Vertical Resolution. J.A.S. 32, pp. 2288-2308.

Swarztrauber, P. and R. Sweet, 1975: Efficient FORTRAN Subprograms for the Solution of Elliptic Partial Differential Equations. NCAR-TN/IA-109.

Wyngaard, J.C. O.R. Cote, and K.S. Rao, 1974: Modeling the Atmospheric Layer. Advances in Geophysics, 18A, Academic Press, New York, pp. 193-212.

END

DATE
FILMED

11-76